Biomedicine & Pharmacotherapy 190 (2025) 118405

Contents lists available at ScienceDirect

Biomedicine & Pharmacotherapy

journal homepage: www.elsevier.com/locate/biopha

Metabolism-targeted therapy in NSCLC – A new theranostics inhalation approach using lactate functionalized and selenium-chrysin loaded nanoparticles (SeChry@PURE$_{G4}$-LA$_{24}$)

Cindy Mendes [a,b], Filipa Martins [a,b], Sara Granja [c,d,e,f], Joana Gonçalves [a], Hélio Barros [g], Teresa Casimiro [h], Ana Aguiar-Ricardo [h], Fernanda Silva [a], Bruna Abreu [a,b], Miguel Cristovão [a,i], Saudade André [a,b], Sofia A. Pereira [a], Fátima Baltazar [e,f], Helena Cabral-Marques [j], Maria Manuela Gaspar [j], Luís G. Gonçalves [k,1,*], Vasco D.B. Bonifácio [g,**,l,1], Jacinta Serpa [a,b,***,1]

[a] NOVA Medical School|Faculdade de Ciências Médicas, Universidade NOVA de Lisboa, Campo dos Mártires da Pátria, 130, Lisboa 1169-056, Portugal
[b] Instituto Português de Oncologia de Lisboa Francisco Gentil (IPOLFG), Rua Prof Lima Basto, Lisboa 1099-023, Portugal
[c] Department of Pathological, Cytological and Thanatological Anatomy, ESS|P.PORTO, Porto 4200-072, Portugal
[d] REQUIMTE/LAQV, Escola Superior de Saúde, Instituto Politécnico do Porto, Rua Dr. António Bernardino de Almeida, Porto 4200-072, Portugal
[e] Life and Health Sciences Research Institute (ICVS), School of Medicine, University of Minho, Campus Gualtar, Braga 4710-057, Portugal
[f] ICVS/3B's - PT Government Associate Laboratory, Braga/Guimarães, University of Minho, Campus de Gualtar, Braga, Portugal
[g] Bioengineering Department, Instituto Superior Técnico, Universidade de Lisboa, Lisbon, Portugal
[h] LAQV-REQUIMTE, Departamento de Química, Faculdade de Ciências e Tecnologia, Universidade NOVA de Lisboa, Campus de Caparica, Caparica 2829-516, Portugal
[i] Centro Hospitalar Universitário Lisboa Central, Hospital de São José, Rua José António Serrano, 1150-199 Lisboa, Portugal
[j] Research Institute for Medicines, (iMed.ULisboa), Faculty of Pharmacy, Universidade de Lisboa, Av. Prof. Gama Pinto, Lisboa 1649-003, Portugal
[k] Instituto de Tecnologia Química e Biológica António Xavier (ITQB NOVA), Avenida da República (EAN), Oeiras 2780-157, Portugal
[l] IBB - Institute for Bioengineering and Biosciences, Instituto Superior Técnico, Universidade de Lisboa, Lisbon, Portugal

ARTICLE INFO

Keywords:
Non-small-cell lung carcinoma (NSCLC)
Metabolic remodeling
Selenium-containing chrysin (SeChry)
Fourth-generation polyurea dendrimer functionalized with lactic acid (PURE$_{G4}$-LA$_{24}$)
Reactive oxygen species (ROS)
Oxidative stress-induced ferroptosis
Metabolism-directed therapy

ABSTRACT

Lung cancer is one of the most lethal cancers globally, primarily due to delayed diagnosis and lack of specific and effective therapy. Increased lactate production and consumption, along with cysteine metabolic reliance, are features identified in NSCLC in our recent studies. Cancer metabolic remodeling leads to excessive ROS production, triggering oxidative stress, promoting angiogenesis, causing cellular and tissue damage, and contributing to various pathophysiological changes. This study aimed to investigate the therapeutic potential of selenium–chrysin (SeChry), a cysteine metabolism inhibitor, and its delivery targeted at MCT1 by encapsulation in fourth-generation polyurea dendrimers functionalized with lactic acid (PURE$_{G4}$-LA$_{24}$), the nanoformulation SeChry@PURE$_{G4}$-LA$_{24}$, in NSCLC. We explored the impact of SeChry nanoformulation on cell death mechanisms, including ferroptosis, and its influence on angiogenesis in *in vitro* and *in vivo* models. SeChry@PURE$_{G4}$-LA$_{24}$ induces cell death through the induction of intracellular ROS and lipid peroxides, resulting in distinct expression patterns of ferroptosis-associated genes across cell lines. Experiments using chicken embryo chorioallantoic membrane (CAM) and mouse orthotopic xenograft models revealed a trend toward decreased tumor growth and angiogenesis with SeChry@PURE$_{G4}$-LA$_{24}$ administration. These findings suggest the potential of

* Corresponding author.
** Corresponding author at: Bioengineering Department, Instituto Superior Técnico, Universidade de Lisboa, Lisbon, Portugal.
*** Corresponding author at: NOVA Medical School|Faculdade de Ciências Médicas, Universidade NOVA de Lisboa, Campo dos Mártires da Pátria, 130, Lisboa 1169-056, Portugal.
E-mail addresses: cindy.mendes@nms.unl.pt (C. Mendes), filipa-martins@nms.unl.pt (F. Martins), saragranja@med.uminho.pt (S. Granja), joana.c.goncalves@nms.unl.pt (J. Gonçalves), helio.barros@tecnico.ulisboa.pt (H. Barros), air@fct.unl.pt (T. Casimiro), teresa.casimiro@fct.unl.pt (A. Aguiar-Ricardo), fernanda.silva@nms.unl.pt (F. Silva), bruna.lara.abreu@gmail.com (B. Abreu), miguelgcristovao@gmail.com (M. Cristovão), sandre@ipolisboa.min-saude.pt (S. André), sofia.pereira@nms.unl.pt (S.A. Pereira), fbaltazar@med.uminho.pt (F. Baltazar), hcmarques@ff.ulisboa.pt (H. Cabral-Marques), manuelagaspar@campus.ul.pt (M.M. Gaspar), lgafeira@itqb.unl.pt (L.G. Gonçalves), vasco.bonifacio@tecnico.ulisboa.pt (V.D.B. Bonifácio), jacinta.serpa@nms.unl.pt (J. Serpa).
[1] Equal contribution

https://doi.org/10.1016/j.biopha.2025.118405
Received 29 May 2025; Received in revised form 14 July 2025; Accepted 29 July 2025
Available online 1 August 2025

SeChry@PURE$_{G4}$-LA$_{24}$ as an innovative therapeutic approach for NSCLC, highlighting its impact on cell death mechanisms and anti-angiogenic effects.

1. Introduction

Lung cancer is the most commonly diagnosed cancer and the leading cause of cancer-related deaths globally, accounting for 11.4 % of all cancer cases and 18.0 % of all cancer deaths in the year 2020 [1]. Non-small-cell lung carcinoma (NSCLC) constitutes approximately 85 % [2] of lung cancer cases and is the primary focus of research. For stage I or II NSCLC, the first-line treatment involves surgical resection of the tumor along with adjuvant therapy [3]. Conversely, as the disease progresses or is diagnosed at stage III or IV, the therapeutic approach transitions towards chemotherapy, radiotherapy, targeted therapy, or immunotherapy [4-6]. Nevertheless, conventional chemotherapeutic agents share common limitations, such as non-specific targeting, low bioavailability, and the emergence of drug resistance, thereby constraining their overall efficacy in cancer treatment [7]. Immunotherapy has brought new hope to NSCLC; however, only 35 % of patients with advanced disease experience improved outcomes [8,9].

Imbalances in redox equilibrium and disrupted redox signaling, common traits in tumors, play crucial roles in malignant progression and treatment resistance [10]. Carcinoma cells, often characterized by persistent high levels of ROS resulting from genetic, metabolic, and microenvironmental alterations, counterbalance this by enhancing their antioxidant capacity [11]. This seemingly paradoxical pro-oxidant shift can drive tumor growth by inducing DNA damage and genomic instability, triggering inflammatory responses, stabilizing HIF1α, and subsequently reprogramming metabolism [12,13]. The sustained production of ROS in malignant cells creates selective pressure, leading to the development of efficient mechanisms for ROS detoxification, providing a survival advantage under pro-oxidizing conditions [14]. Exploiting the dependency of cancer cells on their antioxidant systems becomes crucial for inducing targeted cell death. This involves elevating oxidative stress beyond the toxicity threshold, a strategy that selectively affects cancer cells while sparing normal cells characterized by lower intracellular ROS levels [15]. The dual nature of ROS, functioning both as regulators of cellular physiology and inducers of cytotoxicity, depends on variables like magnitude, duration, and the site of their generation [16]. Understanding and manipulating these intricate processes present avenues for targeted interventions in cancer therapy.

The reciprocal interaction among malignant cells, endothelial cells (ECs), and other microenvironmental components can mutually influence angiogenesis, cell proliferation, tumor growth and dissemination [17]. ROS can selectively activate specific signaling pathways, playing a role in tumor development by regulating cellular proliferation, promoting angiogenesis, and facilitating metastasis [18,19]. Angiogenesis refers to the formation of new blood vessels originating from pre-existing vasculature, playing a crucial role in both normal physiological processes and pathological conditions [20]. Its substantial influence is evident in the progression and metastasis of various types of cancer, namely in NSCLC [21,22]. Elevated levels of ROS, including superoxide and hydrogen peroxide, have been identified as signaling molecules involved in mediating several tumor growth-related responses, such as angiogenesis and mutagenesis [23]. Vascular endothelial growth factor (VEGF), a crucial angiogenesis growth factor, stimulates endothelial cell permeability, proliferation, migration, and tube formation primarily through the VEGF receptor 2 (VEGFR2) [24, 25]. Oxidative stress has been observed to upregulate VEGF expression in tumor cells, contributing to increased microvessel counts and poorer prognosis in various neoplasias [26]. Cancer neoangiogenesis appears to exhibit greater responsiveness to oxidative stress compared to physiological angiogenesis [27]. This heightened sensitivity is attributed to the metabolic remodeling of malignant cells and tumor-associated stromal cells, contributing to the establishment of a pro-oxidative tumor microenvironment [28]. At the molecular level, ROS inhibit prolyl hydroxylases (PHDs), resulting in the stabilization of HIF1α. Consequently, this stabilization leads to the transcription of VEGF and other proangiogenic factors [29,30].

The oxidative stress-dependent generation of lipid peroxides is a fundamental aspect of ferroptosis, a recently discovered process of programmed cell death. In this mechanism, iron ions (Fe^{2+}) undergo a Fenton-like reaction, generate free radicals, and promote lipid peroxidation, elevating ROS levels while depleting intracellular GSH. This depletion, in turn, impairs the activity of glutathione peroxidase 4 (GPX4), a GSH-dependent hydroperoxidase responsible for scavenging lipid peroxides [31,32]. ROS-induced lipid peroxidation directly damages membranous phospholipids and can also function as a cell death signal [33]. Ferroptosis is not strictly confined to cell death but can also be associated with the regulation of various biological and pathophysiological processes, including carcinogenesis [31,34].

We previously reported that selenium–chrysin (SeChry), a modulator of cysteine catabolism and intracellular availability, induced notable metabolic shifts, impacting crucial pathways and key metabolites, thereby contributing to disruptions in redox homeostasis and cellular biosynthesis and ultimately to NSCLC cell death [35]. However, its potential involvement in ferroptosis in NSCLC remains unknown. NSCLC is highly heterogeneous, both at the molecular and histological levels [36]. Despite the diversity in adaptive metabolic profiles among NSCLC cells, the production and consumption of lactate serve as defining features for specific cellular subsets [37]. The movement of lactate across the plasma membranes is primarily facilitated by monocarboxylate transporters (MCTs) belonging to the SLC16 solute carrier family [38,39]. We revealed that the use of SeChry nanoencapsulated in polyurea dendrimers functionalized with lactic acid (SeChry@PURE$_{G4}$-LA$_{24}$), showing specificity to malignant cells expressing MCTs, is a promising treatment approach for NSCLC.

Owing to its distinctive properties, nanodelivery systems prevent therapeutics degradation [40]. These systems not only precisely deliver anticancer drugs to tumor sites but also minimize non-specific harm to the target tissue, thereby enhancing anticancer efficacy [41-44]. Nanocarrier-based drug delivery represents a novel strategy for NSCLC treatment, offering benefits such as improved drug bioavailability in the body, enhanced safety through site-specific drug delivery, and the ability for sustained and controlled release during targeted drug delivery [45-47]. Moreover, inhalation nano-based drug delivery systems represent an emerging therapy offering a new way to treat NSCLC. Inhalation chemotherapy presents notable advantages over intravenous chemotherapy, as the lungs provide optimal conditions for efficient mass transfer, facilitating drug permeation into the bloodstream [48]. Furthermore, it reduces the clinical response time and systemic/whole body exposure to drugs, thereby minimizing side effects and adverse reactions [49]. Consequently, dry powder formulations containing SeChry@PURE$_{G4}$-LA$_{24}$ nanoparticles for pulmonary delivery could serve as an innovative therapeutic approach in the treatment of NSCLC.

Here, we explored the therapeutic potential of SeChry and SeChry@PURE$_{G4}$-LA$_{24}$ in NSCLC, focusing on their effects on malignant cell death mechanisms, including ferroptosis, and their influence on angiogenesis in both *in vitro* and *in vivo* models. The use of encapsulated SeChry (SeChry@PURE$_{G4}$-LA$_{24}$) addresses its inherent toxicity toward non-cancerous cells, as demonstrated in our previous studies with nanoparticles functionalized with folate [50,51]. By loading SeChry into lactate-functionalized nanoparticles, we achieved two critical objectives: first, we reduced off-target toxicity; second, we enhanced selective delivery to cancer cells, which overexpress monocarboxylate

transporters (MCTs) compared to normal cells.

2. Materials and methods

Cell lines and culture conditions

Human adenocarcinoma cell lines A549 (CCL-185™, ATCC), H1975 (CRL-5908™, ATCC), and H522 (CRL-5810™, ATCC), adenosquamous carcinoma cell line H596 (HTB-178™, ATCC) and mucoepidermoid carcinoma cell line H292 (CRL-1848™, ATCC) were obtained from American Type Culture Collection (ATCC, Manassas, VA, USA) and adenocarcinoma cell line PC-9 (90071810, ECACC) was obtained from European Collection of Authenticated Cell Cultures (ECACC, Porton Down, Salisbury, United Kingdom). The selected NSCLC cell lines present different mutational profiles for *EGFR* and *KRAS*: A549 cells (*EGFR* WT and *KRAS* c.34 G > A (p.Gly12Ser); H292 cells (*EGFR* WT and *KRAS* WT), PC-9 cells (*EGFR* exon 19 deletion (Ex19Del; Glu746-Ala750 deletion) and *KRAS* WT). The cell lines represent the main NSCLC histological types: LUAD (A549 and PC-9) and LUSC (H292). Cells were cultured in Dulbecco's Modified Eagle's Medium 1 × (DMEM) (41965–039, Gibco, Life Technologies) supplemented with 10 % fetal bovine serum (FBS; S 0615, Merck), 1 % Antibiotic-Antimycotic (AA; P06–07300, PAN Biotech) and 50 μg/mL Gentamicin (15750–060, Gibco, Life Technologies). HUVECs (CRL-1730, ATCC) were cultured in Endothelial Cell Growth Basal Medium-2 (EBM-2: CC-3156, Lonza, Bioscience) supplemented with EGM-2 SingleQuots Supplements (CC-4176, Lonza, Bioscience), on 0.2 % gelatin-coated plates or flasks. All experiments with the HUVECs were performed until passage 10.

All cell lines were maintained at 37 ºC in a humidified environment with 5 % CO_2. Cells were cultured until they reached an optical confluence of 75–100 %, and detachment was performed with 0.05 % trypsin-EDTA 1 × (25300–054, Invitrogen). Before any *in vitro* experiment, cells were synchronized under starvation (FBS-free culture medium) overnight, except for cytotoxicity assays. NSCLC cells were kept in control conditions or exposed to SeChry or SeChry@PURE$_{G4}$-LA$_{24}$ for 48 h for cytotoxic assays. The concentrations for each cell line were chosen according to the previously determined half-maximum effective concentrations (EC_{50}) [35,50], for SeChry, A549 (5 μM), H292 (10 μM), and PC-9 (23 μM); and for SeChry@PURE$_{G4}$-LA$_{24}$, A549 (100 μM), H292 (50 μM), and PC-9 (43 μM). HUVECs were exposed to SeChry (12.5 μM) and SeChry@PURE$_{G4}$-LA$_{24}$ (25 μM) based on the determined EC_{50s} (Supplementary Fig. 1). HUVECs were also exposed to filtered conditioned media (CM) from H292 and PC-9 cells previously treated with SeChry and SeChry@PURE$_{G4}$-LA$_{24}$ for 48 h. In some assays, HUVECs were exposed to lactate or CM from NSCLC cells treated with lactate for 24 h. In some assays, cells were pre-treated with the apoptosis inhibitor ZVAD-FMK (MedChemExpress, HY-16658B, 50 μM), or the ferroptosis inhibitor ferrostatin-1 (Fer-1; Sigma-Aldrich, SML0583, 1 μM) for 2 h before the addition of SeChry or SeChry@PURE$_{G4}$-LA$_{24}$.

2.1. Synthesis of PURE$_{G4}$-LA$_{24}$ nanoparticles

Lactic acid-targeted polyurea dendrimer generation four (PURE$_{G4}$-LA$_{24}$) was prepared by reacting polyurea dendrimer generation four (PURE$_{G4}$), obtained using a supercritical-assisted polymerization protocol [52], with activated lactic acid succinic ester (LA-NHS). LA-NHS was synthesized according to the literature [53]. Typically, in a round-bottom flask, 41 mg (0.456 mmol) of lactic acid (LA) was dissolved in dry DMF (5 mL). After the addition of 105 mg (0.908 mmol) of *N*-hydroxysuccinimide (NHS), 103.6 mg (0.502 mmol) of *N,N'*-dicyclocarbodiimide (DCC), and 0.140 mL (1.04 mmol) of triethylamine (TEA), the reaction was stirred at RT overnight in the dark. After this period, TEA was evaporated and 150 mg (0.019 mmol) of PURE$_{G4}$ in dry DMF (0.75 mL) and 0.140 mL (1.04 mmol) of TEA were added and allowed to react overnight.

The mixture was then filtered to remove precipitated solids and TEA was evaporated. The solution was then dialyzed (MWCO 100–500 Da), and the recovered solution was washed several times with diethyl ether to remove residual DMF. After water evaporation, 194 mg (quantitative yield) of the product was obtained as a light-yellow sticky oil. By ^{1}H-NMR analysis a total of 24 lactate molecules (50 %, PURE$_{G4}$ has 48 available reacting amines at the surface) were incorporated on the dendrimer surface (Supplementary Fig. 2). ^{1}H-NMR (400 MHz, D_2O) δ (ppm): 4.08 (24H, q, *J*= 8.0 Hz, CH lactate), 3.33–3.17 (280H, m, dendrimer), 2.99 (bs, OH lactate), 2.83 (bs, OH lactate), 2.76–2.61 (360H, m, dendrimer), 1.96 (bs, NH dendrimer), 1.30 (72H, d, *J*= 8.0 Hz). Further characterization of single particle size and charge (DLS measurements using diluted solutions) was precluded by the formation of aggregates in aqueous solution (mean size ~396 nm, ζ = +5.1 ± 0.4 mV). We attribute this behaviour to intermolecular hydrogen bonding among surface lactates. In contrast to the behaviour of typical colloidal particles, dendrimer aggregation in aqueous solution is more pronounced at low ionic strengths, attributed to the interpenetration of dendrimer branches at low ionic strengths [54].

2.2. Preparation of the SeChry@PURE$_{G4}$-LA$_{24}$ nanoformulation

SeChry was encapsulated in PURE$_{G4}$-LA$_{24}$ nanoparticles following a modified protocol [55]. Briefly, a $CHCl_3$ solution (0.5 mL) of SeChry (6.5 mg) was added to an aqueous solution (2 mL) of PURE$_{G4}$-LA$_{24}$ (125 mg). Next, $CHCl_3$ was removed in a rotary evaporator, and the mixture was allowed to stir at RT overnight. Then, the aqueous solution was extracted with $CHCl_3$ to remove non-encapsulated SeChry. No SeChry was found in the $CHCl_3$ extracts (control by thin-layer chromatography, TLC), thus confirming a full encapsulation, and indicating passive, hydrophobic partitioning into the dendrimer. A maximum drug: dendrimer ratio matching the loading observed for other small hydrophobic cargos in PURE$_{G4}$ systems was maintained. We have previously shown that small-molecule release from PURE$_{G4}$ dendrimers follows a Fickian diffusion, with *ca.* 90 % of payload released within 8 h [55].

2.3. Preparation of nano-in-micro SeChry@PURE$_{G4}$-LA$_{24}$ dry powder

The preparation of the dry powder for *in vivo* inhalation studies followed our reported protocol [56]. Briefly, 3.6 g of chitosan (CHT) were dissolved in acidic water (acetic acid 1 % v/v) under stirring for 24 h. The solution was filtered, and 525 mg of the SeChry@PURE$_{G4}$-LA$_{24}$ (containing 50 mg of encapsulated SeChry) previously dissolved in 20 mL of ethanol were added. The mixture was homogenized under stirring and fed to a laboratory-scale of the supercritical assisted spray drying (SASD) apparatus. The atomized particles from the flow stream were collected at the bottom of the cyclone in a suitable container (m= 0.795 g). The same procedure was used to prepare the control particles, using CHT (3.3 g) and PURE$_{G4}$-LA$_{24}$ (447 mg dissolved in 20 mL of ethanol) (m= 1.041 g). As described [55], the nanoformulation prepared according to this protocol presents the emitted doses (EDs) ranging from 99.1 ± 0.3 % to 99.6 ± 0.4 %, indicating excellent aerosolization efficiency. The fine particle fraction (FPF), representing the proportion of particles capable of reaching the alveolar region (deep lung), is about 28 %. These values are consistent with those reported for a commercially available dry powder inhaler (DPI) [57].

2.4. Cell death analysis

Cell death was assessed by flow cytometry. Cells (2×10^5 cells/mL) were seeded in 24-well plates and exposed to specific conditions. After the experimental conditions, supernatants were collected, and cells were harvested with trypsin. The cells, along with the supernatant, were then centrifuged at 150 × g for 2 min. Cells were suspended with 0.5 μL Annexin V-fluorescein (FITC) - (640906, BioLegend) in Annexin V binding buffer 1 × (10 mM HEPES pH 7.4; 391333, Millipore), 140 mM sodium chloride (NaCl; 106404, Merck), 2.5 mM calcium chloride ($CaCl_2$; 449709, Sigma-Aldrich) and incubated at RT, in the dark for

15 min. After incubation, samples were resuspended in 200 µL PBS 1 × 0.1 % (v/w) BSA and centrifuged at 155 × g for 2 min. Cells were resuspended in 100 µL of Annexin V binding buffer 1 × and 2.5 µL propidium iodide (PI, 50 µg/mL; P4170, Sigma-Aldrich) was added and samples were analyzed by flow cytometry (FACScalibur – Becton Dickinson), using *FlowJo* v10.0.7 software (https://www.flowjo.com). Experiments were performed in biological triplicates.

2.5. Reactive oxygen species (ROS) quantification by flow cytometry

NSCLC cells (5 × 10^4 cells/well) were plated in 24-well plates. The intracellular ROS were detected in cells incubated with 10 mM DCF-DA probe (D6883, Sigma Aldrich), and mitochondrial ROS were detected in cells incubated with 5 mM MitoSox Red probe (M36008, Invitrogen), both at 37 °C for 30 min. The acquisition was performed with FACScalibur (Becton Dickinson), and data was analyzed with *FlowJo X* v10.0.7 software (https://www.flowjo.com).

2.6. Lipid peroxide quantification by flow cytometry

NSCLC cells (5 × 10^4 cells/well) were plated in 24-well plates. After experimental conditions, cells were incubated with 2 mM C11-Bodipy 581/591 (D3861, Invitrogen), for 30 min at 37 °C in the dark. The excess dye was removed by washing with 2 % FBS-1X PBS, and cell pellets were resuspended in 2 % FBS-1 × PBS for acquisition by flow cytometry (FACScalibur – Becton Dickinson). *FlowJo X* v10.0.7 software (https://www.flowjo.com) was used to analyze data.

2.7. Quantitative real-time PCR (qPCR)

NSCLC cells were plated in 12-well plates (1 × 10^5 cells/well/mL) and after exposure to the experimental conditions, the total RNA was extracted using the RNeasy Mini Extraction kit (74104, Qiagen, Hilden, Germany) and cDNA synthesized from 1 µg RNA by SuperScript II Reverse Transcriptase (18080044, ThermoFisher Scientific), according to the manufacturers' protocols and cDNA was synthesized as mentioned above. qPCR was performed using SYBR Green PCR Master Mix (04707516001, Roche), according to the manufacturer's protocol. Real-time PCR was carried out during 40 amplification cycles, according to the manufacturer's instructions, using a Lightcycler® 480 System instrument (05015243001, Roche). The transcriptional expression of genes encoding prostaglandin-endoperoxide synthase 2 (PTGS2), glutathione peroxidase 4 (GPX4), and glutathione synthetase (GSS) was evaluated, using the primers: PTGS2 (Fwd: CTGGCAGGGTTGCTGGTG; Rev: CATCTGCCTGCTCTGGTC); GPX4 (Fwd: GCAGGAGCCAGGGAGTAAC; Rev: CCTTGGGTTGGATCTTCATCC), and GSS (Fwd: GAGAGAGGGTGGAGGTAAC; Rev: CCATGAGGATGTAGGAGGCC). HPRT (Fwd: TGACACTGGCAAAACAATGCA; Rev: GGTCCTTTTCACCAGCAAGCT) was used as a housekeeping gene.

2.8. High-Performance Liquid Chromatography (HPLC)

The effect of free and encapsulated SeChry on cysteine (Cys) uptake and GSH content was tested in NSCLC cells by HPLC with fluorescence detection (FLD) (Shimadzu Scientific Instruments Inc., Columbia, MD, USA). Total intracellular thiol levels were assessed according to our previous studies [51]. The chromatographic conditions were optimized, and the detector excitation and emission wavelengths were set to 385 and 515 nm, respectively. The chromatographic separation was performed by isocratic elution of mobile phase, consisting of 100 mM acetate buffer (pH 4.5) and methanol (98:2 (v/v)), for 20 min, at a flow rate of 0.6 mL/min. Cells (2.5 × 10^5 cells/mL) were cultured in six-well plates (2 mL/well) and exposed to free or encapsulated SeChry for 24 h. After this period, cells were collected with 0.05 % trypsin-EDTA, centrifuged at 255 × g for 2 min, washed twice in PBS (1 ×), and lysed with 60 µL of PBS (1 ×) with 0.01 % (v/v) Triton X-100. Cell lysates were centrifuged at 10,600 × g for 2 min and stored at −80 °C. The total thiol fraction was obtained by reducing the sulfhydryl groups with TCEP (100 g/L, 5 µL). After 30 min of incubation at room temperature, the samples were treated with TCA (100 g/L containing 1 mM EDTA, 45 µL) for protein precipitation. The mixture was then vortexed and centrifuged (13,000 × *g*, 10 min, 4 °C) and the supernatant collected (25 µL) to a new tube, containing NaOH (1.55 M, 5 µL), $Na_2B_4O_7{\cdot}10H_2O$ (pH 9.5, 125 mM with 4 mM EDTA, 62.5 µL), and SBD-F (1 g/L in $Na_2B_4O_7$ buffer, 25 µL). The final mixture was vortexed and incubated in the dark, at 60 °C for 1 h, to complete the derivatization of the free sulfhydryl groups. Lastly, 25 µL of the final volume obtained were injected into the HPLC system. For the HPLC analyses, a reversed-Phase C18 LiChroCART 250–4 column (LiChrospher 100 RP-18, 5 µm, VWR) was used, in a column oven at 29 °C on isocratic elution mode for 20 min, at a flow rate of 0.8 mL/min. The mobile phase consisted of 100 mM acetate buffer (pH 4.5) and methanol (99:1 (*v/v*)). The detection was performed with RF 10AXL fluorescence detector, operating at excitation and emission wavelengths of 385 and 515 nm, respectively. The measured thiol levels were normalized by protein level.

2.9. Enzyme-linked immunosorbent assay ELISA

H292 and PC-9 cells (2 × 10^7 cells/mL) were plated in 175 cm^2 culture flasks (T175) and exposed to SeChry SeChry@$PURE_{G4}$-LA_{24} for 48 h. Non-adherent cells were collected, and adherent cells were scraped from the culture flask. Pellets were solubilized in chilled 1 × Cell Extraction Buffer PTR, incubated on ice for 20 min, and centrifuged at 18,000 × g for 20 min at 4°C. For GPX4 quantification, the cell lysates were analyzed via the Human GPX4 ELISA Kit (ab304936; Abcam). After sample addition, capture and detection antibodies were applied, followed by TMB substrate for color development. The reaction was stopped, and the absorbance was also measured at 450 nm, with GPX4 levels determined via a standard curve.

2.10. Wound-healing assay

HUVECs were plated in 24-well plates (1 × 10^5 cells/well) until a confluent monolayer formed. Once confluent, cells were incubated for 3 h with 5 mg/mL mitomycin-C (M4287, Sigma Aldrich), and a linear scratch was made in each monolayer using a P200 pipette tip, to create a wound across the well diameter. The media was replaced to remove debris and suspended cells, and the experimental conditions were added. Bright-field images of each well were captured using the Olympus IX53 Inverted Microscope at the following time points: 0, 2, 4, 6, 8, 10 and 24 h. Wound closure was quantified using *ImageJ* software (imagej.nih.gov/ij).

2.11. Tube-forming assay

A 48-well plate was coated with 100 µL of matrigel (354230, Corning) and incubated at 37°C for 30 min until solidification. HUVECs were then incubated with 2 mg/mL of calcein (C1430, Invitrogen), a fluorescent cell-permeable dye, for 30 min at 37 °C and 5 % CO_2 and seeded at a density of 3 × 10^4 cells/well on top of the matrigel. The cells were exposed to the experimental conditions for 6 h, and representative images of the formed tube-like structures were acquired using an Olympus IX53 Inverted Microscope and analyzed with *ImageJ* software (imagej.nih.gov/ij). The density of vessel-like structure formation (branch points number/mm^2) was calculated as representative of vascular density.

2.12. Cancer cell endothelial adhesion

In a 24-well plate, calcein labelled-H292 and PC-9 cells (5 × 10^4 cells/well) were seeded on top of an HUVECs (1 × 10^5 cells/well) monolayer pretreated with 100 ng/mL TNFα (H8916, Sigma-Aldrich), for 24 h. H292 and PC-9 cells were incubated with HUVECs

(previously exposed to TNFα and experimental conditions) for 40 min, at 37 °C in a humidified environment with 5 % CO_2. Non-adherent cells were removed by washing with PBS 1 × and images were acquired using an Olympus IX53 Inverted Microscope and analyzed using *ImageJ* software (imagej.nih.gov/ij). Three fields in each well were evaluated at 10 × magnification.

2.13. Transendothelial cancer cell migration

HUVECs (5 × 10^4 cells/well) were plated in 8 μm pore transwells (upper wells) (3422, Corning) and exposed to 100 ng/mL TNFα for 24 h, and to experimental conditions for 16 h. H292 and PC-9 cells previously plated under starvation using serum-free DMEM, for 24 h, were incubated with calcein (2 mg/mL) and seeded (1.5 × 10^4 cells/well) in serum-free DMEM on top of the HUVECs monolayer, for 5 h. Complete media was added to the lower well and used as a chemoattractant. Cells on the upper Transwell® surface were removed with a cotton swab, and the invading H292 or PC-9-calcein-labeled cells were photographed on an Olympus IX53 Inverted Microscope. Three fields in each well were counted (10 × magnification) using the *ImageJ* software (imagej.nih.gov/ij).

2.14. Immunofluorescence

In the immunofluorescence assay, cells (1 ×10^5 cells/well) were seeded on glass slides coated with 0.2 % gelatin until 80 % confluence and then fixed in 2 % paraformaldehyde for 15 min at 4 ºC. Cells were incubated with anti-xCT (1:100, ab175186) and anti-integrin alpha 6 (1:100, AB20142, Abcam) overnight at 4 °C. Alexa Fluor® 488 anti-mouse (A-11001, Invitrogen) and Alexa Fluor® 488 goat anti-rabbit (A-11034, Thermo Fisher) were the secondary antibodies used. The slides were mounted in VECTASHIELD media with DAPI (4′-6-diamidino-2-phenylindole) (Vector Labs) and examined by standard fluorescence microscopy, using a Zeiss Imajer.Z1 AX10 microscope. Images were acquired and processed with CytoVision software (https://cytovision-genus.software.informer.com). Signal quantification was performed with ImageJ software (https://imagej.nih.gov/ij/download.html).

2.15. Mitochondrial membrane potential (MMP)

The MMP was measured in H292 and PC-9 cell lines using JC-1 (M34152, Molecular Probes, Life Technologies). Cells (5 ×10^5 cells/well) were seeded in 24-well plates and cultured under control conditions, then exposed to SeChry SeChry@$PURE_{G4}$-LA_{24} for 48 h. Cells were then incubated for 30 min with 5 μM JC-1 (37°C, 5 % CO2). A positive depolarized control was used, in which cells were previously incubated with 50 μM CCCP for 5 min (37°C, 5 % CO2) and then incubated with JC-1. Acquisition was performed in a FACScalibur (Becton Dickinson). Data were analyzed with *FlowJo X* v10.0.7 software (https://www.flowjo.com).

2.16. Ex vivo chick chorioallantoic membrane (CAM) assay

Fertilized chicken eggs were incubated in a 40 % humidified atmosphere at 37 ºC. On day 3 of embryo development, a window was made into the eggshell, sealed with tape, and the eggs were returned to the incubator. On day 9 of embryo development, an H292 and PC-9 cell line suspension (2 × 10^6 cells) in 10 μL of Matrigel (Corning: 354230) was placed inside the eggs to allow the formation of a 3D tumor. On day 13 of development, the tumors were treated with 20 μL of $PURE_{G4}$-LA_{24} (control group) and SeChry@$PURE_{G4}$-LA_{24}. H292 cells were treated with 100 μM SeChry@$PURE_{G4}$-LA_{24}, along with an equivalent dose of PURE@$_{G4}$.LA_{24}. PC-9 cells received 200 μM SeChry@$PURE_{G4}$-LA_{24}, along with an equal concentration of empty nanoparticles. After 96 h of treatment (day 17 of development), the chicken embryos were sacrificed by placing them at −80 ºC for 10 min. Digital images of the tumors were taken on days 13 and 17 of development in a stereomicroscope (Olympus S2 × 16), using a digital camera (OlympusDP71). At the selected time points, the "*in ovo*" tumor area was measured using the *ImageJ* software. Results were expressed as the area difference between day 13 and 17. For blood vessel analysis, "*ex ovo*" images were analyzed in *Fiji* software using the "Vessel analysis" plugin, and the results were expressed as a percentage of blood vessel area. The tumors were fixed in 4 % paraformaldehyde at RT and embedded in paraffin for further analysis.

2.17. Xenograft lung cancer NOD.Cg-Prkdcscid Il2rgtm1Wjl/SzJ murine models

Xenograft orthotopic mice models of NSCLC were induced by tail vein injection of H292 and PC-9 cells (1 ×10^6 cells/200 μL/mouse), in 6-week-old NSG (NOD.Cg-*Prkdc*^{scid} *Il2rg*^{tm1Wjl}/SzJ) immunocompromised male mice, obtained from Charles River Laboratory (Barcelona, Spain). Animals were housed in individually ventilated cages, under strict hygiene conditions, with a cycle of light/dark of 12 h, temperature of about 20–24°C, and relative humidity of 50–65 %. Moreover, the animals had free access to a sterilized diet and acidified water. Animal studies were carried out in agreement with the animal welfare organ (ORBEA) of the Faculty of Pharmacy of the University of Lisbon, approved by the competent national authority *Direção Geral de Alimentação e Veterinária* (DGAV) and in accordance with the national (DR 113/2013, 2880/2015, 260/2016 and 1/2019) and European (2010/63/EU) legislation for the use and care of animals in research.

Mice's body weight was evaluated at least 2 times per week, and general behavior and symptomatology were also registered. After 38 days post-cell injection, pulmonary administration of the dry powder formulations containing $PURE_{G4}$-LA_{24} (control) or SeChry@$PURE_{G4}$-LA_{24} nanoparticles was performed using a simple apparatus based on a 15 mL centrifuge tube where dry powder (20 mg) of each formulation was inserted [58]. A small hole was made in the bottom of the tube to allow the powder delivery to the mouse. A plastic pump connected to the upper part of the tube allowed the production of a turbulent air stream for fluidizing the powder. Each mouse was restrained in a 50 mL tube having a small hole in the bottom. The lower part of the 50 mL tube was connected to the 15 mL tube using a baby bottle teat. The dry powder (20 mg) was inserted into the device and each animal received the formulation by inhalation for 2 min. Mice were administered spray-dried microparticles a total of four times over the course of one week using the device described above. Both the control $PURE_{G4}$-LA_{24} and SeChry@$PURE_{G4}$-LA_{24} nanoformulations were administered in groups of four mice. Taking into account that 795 mg of SeChry@$PURE_{G4}$-LA_{24} nanoparticles were effectively loaded with 9.6 mg SeChry, that each mouse was exposed to 20 mg of dry powder and less than 10 % of this powder was inhaled (data not shown); this means that the administered dose of SeChry@$PURE_{G4}$-LA_{24} was 0.93 mg/kg of body weight. Animals were euthanized on day 47 after injection (2 days after the last administration) and lung, liver, and spleen tissues were collected, fixed in 10 % formalin, and embedded in paraffin. The tissues were then serially sectioned (3 μm), deparaffinized, and stained with hematoxylin and eosin (H&E). The histological evaluation was conducted by two pathologists and the percentage of tumor area was calculated in the H&E-stained lung sections using *QuPath* software (https://qupath.github.io/).

2.18. ^{1}H-NMR profiling of peripheral blood serum from mice

The blood serum collected was evaluated by ^{1}H-NMR spectroscopy. Sera were diluted in a buffer of 100 mM KPi (pH 7) with TSP (0.16 mM) and transferred to NMR match tubes of 2.5 mm (16545, Bruker), using 70 μl sera + 70 μl KPi buffer. Spectra were acquired in a 500 MHz magnetic field in a 500 UltraShield™ Spectrometer (Bruker) equipped

with a 5 mm TCI C/N Prodigy Cryo probe at 25°C. For each sample three ^{1}D 1H-NMR spectra were acquired: one with a *noesypr1d* pulse sequence as a sum of 64 free induction decays (FIDs) (48 K of Time-Domain (TD), 11.76 ppm of spectral window (SW), 1 s relaxation delay and 10 ms of mixing time); another with a *cpmgpr1d* as a sum of 64 FIDs (64 K TD, 20 ppm SW, 4 s relaxation delay, an echo time of 0.2 ms and 300 repetitions of the echo time per scan); and diffusion edited pulse experience (*ledbpgppr2s1d)* as a sum of 64 FIDS (64 k TD, 30 ppm SW, 4 s relaxation delay and a diffusion time of 0.2 ms). Spectra were acquired and processed using Topspin 3.6. NMRProcFlow 1.4 software (nmrprocflow.org) was used for further spectra processing and to define the spectra buckets that were analyzed by MetaboAnalyst 6.0 (accessed on 28 February 2024). All data obtained from NMRProcFlow were normalized through Constant Sum Normalization.

2.19. Statistical analysis

Statistical analysis was conducted using *GraphPad Prism* 6.0 software (https://www.graphpad.com). Sample data were presented as the mean (normal distribution) ± SD. Assays were performed with a minimum of three biological replicates per treatment. Statistical comparisons between groups were performed using a two-tailed unpaired Student's *t*-test, and multiple comparisons were analyzed using One-way ANOVA with Dunnett's or Tukey's test. For comparisons between two groups, a two-tailed independent-samples *t*-test was used. Differences between experimental conditions were considered statistically significant at $p < 0.05$.

3. Results

3.1. SeChry@PURE$_{G4}$-LA$_{24}$ promotes cell death through ROS induction and lipid peroxidation

Cells were exposed to SeChry or SeChry@PURE$_{G4}$-LA$_{24}$ for 48 h, with concentrations for each cell line selected based on the previously determined EC$_{50}$ [50]. A549 and H292 cells exhibited higher sensitivity to encapsulated SeChry nanoparticles compared to free SeChry (Fig. 1 A). Conversely, PC-9 cells demonstrated greater sensitivity to free SeChry. In addition, our findings revealed that cell death in A549 and H292 cells exposed to SeChry primarily occurred through early apoptosis plus late apoptosis+necrosis, and necroptosis, whereas in all cell lines treated with SeChry@PURE$_{G4}$-LA$_{24}$, it predominantly resulted in necrosis and necroptosis (Fig. 1B).

Since SeChry is known as a cystathionine-β-synthase (CBS) inhibitor

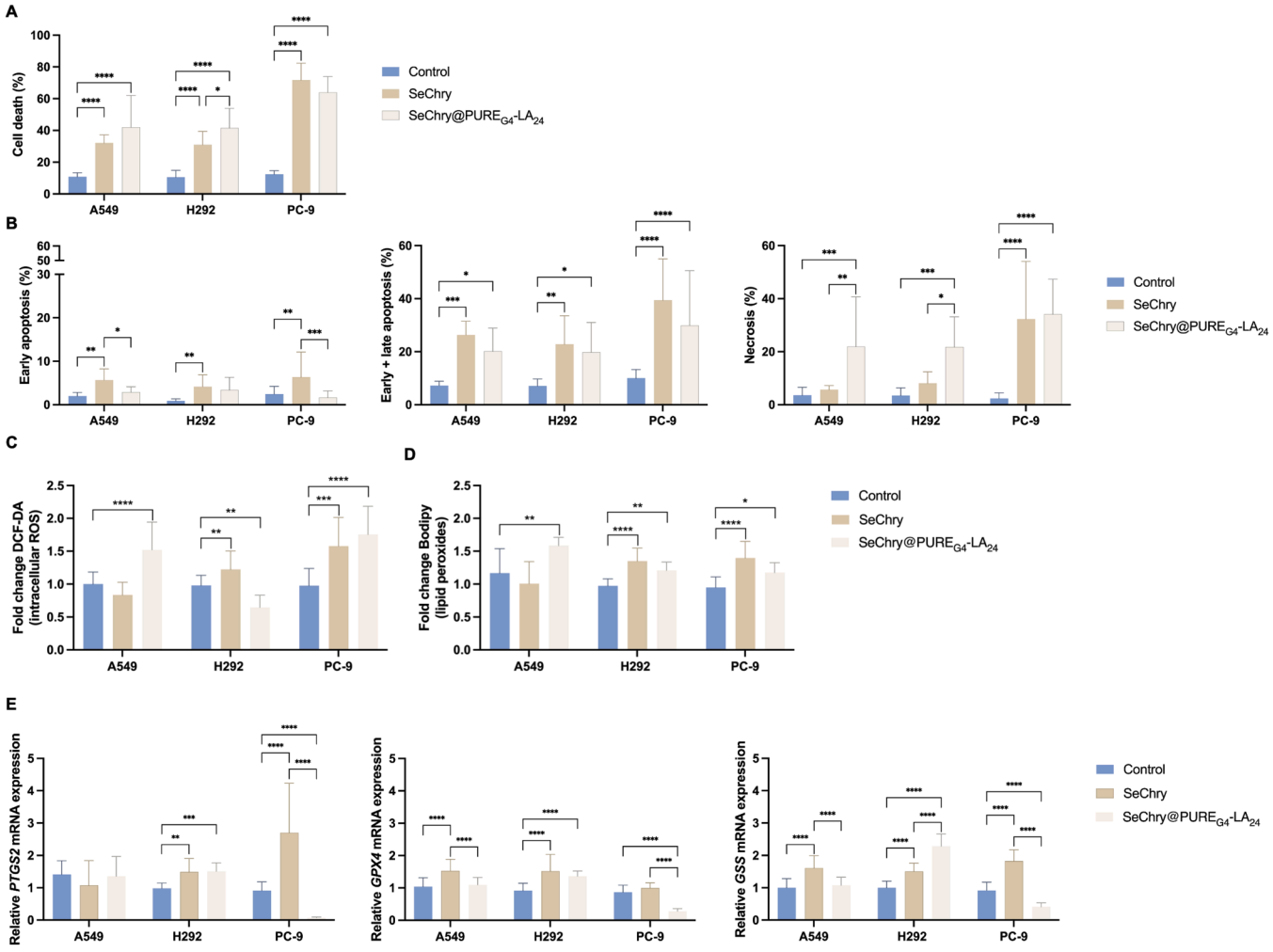

Fig. 1. Free or encapsulated SeChry induces increased early and/or late apoptosis or necrosis and augments intracellular ROS and lipid peroxide levels. Exposure of A549, H292 and PC-9 cells to SeChry/SeChry@PURE$_{G4}$-LA$_{24}$ for 48 h. Concentrations used were: SeChry, A549 (5 μM), H292 (10 μM), and PC-9 (23 μM); and SeChry@PURE$_{G4}$-LA$_{24}$, A549 (100 μM), H292 (50 μM), and PC-9 (43 μM). (A) Percentage of cell death analyzed by flow cytometry using Annexin V and PI in A549, H292 and PC-9 cells. (B) Percentage of early apoptosis, early+late apoptosis and necrosis. Levels of (C) intracellular ROS (DCF-DA) and (D) lipid peroxides (C11-Bodipy) analyzed by flow cytometry. (E) mRNA expression analysis of ferroptosis-associated genes PTGS2, GPX4 and GSS. Data is represented as mean ± SD. *p < 0.5, **p < 0.01, ***p < 0.001, ****p < 0.0001 (two-way ANOVA with Tukey's test was used).

[51], theoretically leading to imbalanced intracellular antioxidant potential, we investigated the impact of exposure to SeChry@PURE$_{G4}$-LA$_{24}$ on intracellular levels of ROS and lipid peroxides. SeChry notably elevated ROS levels in H292 and PC-9 cells, while SeChry@PURE$_{G4}$-LA$_{24}$ induced a significant increase in intracellular ROS in A549 and PC-9 cell lines (Fig. 1 C). We also noted that free SeChry led to a considerable increase in mitochondrial ROS specifically in H292 cells but only tended to increase mitochondrial ROS in the other 2 cell lines (Supplementary Fig. 3). Additionally, SeChry triggered a significant rise in lipid peroxide levels in H292 and PC-9 cells, whereas SeChry@PURE$_{G4}$-LA$_{24}$ increased lipid peroxides significantly in all three cell lines (Fig. 1D).

After considering these findings, we proceeded to assess the expression of genes associated with ferroptosis following treatment with SeChry@PURE$_{G4}$-LA$_{24}$. Free SeChry led to an overexpression of *PTGS2* in H292 and PC-9 cells, while SeChry@PURE$_{G4}$-LA$_{24}$ upregulated this gene exclusively in H292 cells (Fig. 1E). *GPX4* expression levels were significantly increased in A549 and H292 cells following SeChry treatment. In contrast, SeChry@PURE$_{G4}$-LA$_{24}$ led to a significant downregulation of *GPX4* in PC-9 cells, while the opposite effect was observed in H292 cells. The expression of *GSS* was elevated in A549, H292, and PC-9 cells treated with SeChry. SeChry@PURE$_{G4}$-LA$_{24}$ significantly increased *GSS* in H292 cells but decreased it in PC-9 cells. Thus, exposure to SeChry@PURE$_{G4}$-LA$_{24}$ not only amplified intracellular ROS and lipid peroxide levels but also induced differential expression patterns of ferroptosis-associated genes across NSCLC cell lines, suggesting a complex interplay in modulating ferroptosis mechanisms that warrants further investigation for potential therapeutic implications.

3.2. SeChry@PURE$_{G4}$-LA$_{24}$ induces cell death via disruption of the cystine–cysteine–GSH–GPX4 axis

Given the observed alterations in ferroptosis-associated gene expression, we next sought to determine whether SeChry-induced cell death involves ferroptosis and occurs independently of classical apoptotic pathways. Cells were treated with free or encapsulated SeChry, alone or in combination with the pan-caspase inhibitor ZVAD-FMK. In H292 and PC-9 cells, co-treatment with ZVAD-FMK did not cause any significant changes in cell death, suggesting that SeChry induces a form of cell death that is at least partially caspase-independent (Fig. 2 A). Given the limited rescue by ZVAD-FMK, we next investigated its effect on lipid peroxidation. Lipid peroxide levels were higher following SeChry treatment and remained similarly elevated in the presence of ZVAD-FMK (Fig. 2B). These results indicate that lipid peroxidation occurs independently of caspase activity, further supporting the hypothesis of ferroptotic cell death. To confirm the involvement of ferroptosis, cells were co-treated with Ferrostatin-1 (1 μM), a ferroptosis-specific inhibitor. Co-treatment significantly decreased cell death induced by SeChry and SeChry@PUREG4-LA$_{24}$ in both H292 and PC-9 cells (Fig. 2 C), and lipid peroxide levels were also significantly reduced upon Ferrostatin-1 treatment (Fig. 2D), indicating that SeChry-induced cytotoxicity is at least partially mediated by ferroptosis.

To further investigate ferroptosis-related mechanisms, we analyzed the expression and activity of key regulators in the cystine–cysteine–GSH–GPX4 axis. Immunofluorescence analysis revealed a significant reduction in xCT expression in H292 cells following treatment with SeChry@PURE$_{G4}$-LA$_{24}$ (Fig. 2E and F). In PC-9 cells, xCT expression also showed a decreasing trend with SeChry@PURE$_{G4}$-LA$_{24}$, suggesting that SeChry@PURE$_{G4}$-LA$_{24}$ modulates xCT expression in both cell lines, with a more significant effect in H292 cells. Measurement of intracellular cysteine levels showed a modest tendency to increase in H292 cells at 48 h with both treatments, while PC-9 cells exhibited an increase in cysteine at 48 h after SeChry@PURE$_{G4}$-LA$_{24}$ treatment (Fig. 2 G). Despite this, total GSH levels tended to decline in both cell lines in PC-9 at 48 h (Fig. 2 H). The GSH/cysteine ratio (Fig. 2I) was significantly decreased in H292 cells at both 24 and 48 h with SeChry@PURE$_{G4}$-LA, and in PC-9 cells at 48 h with both free and encapsulated SeChry, suggesting a low cysteine utilization for GSH synthesis. Because GPX4 is a key enzyme detoxifying lipid peroxides and protecting against ferroptosis [32], we quantified GPX4 protein levels using ELISA. GPX4 protein levels were elevated in both cell lines, particularly in PC-9 cells treated with SeChry@PURE$_{G4}$-LA$_{24}$ (Fig. 2 J), suggesting a potential compensatory response to increased lipid peroxidation. Considering the involvement of mitochondrial dysfunction in oxidative stress and non-apoptotic cell death pathways such as ferroptosis, we assessed mitochondrial membrane potential (Δψm) to determine whether mitochondrial impairment contributes to SeChry- and SeChry@PUREG$_4$-LA$_{24}$-induced cytotoxicity. Both SeChry and SeChry@PURE$_{G4}$-LA$_{24}$ significantly reduced Δψm in H292 and PC-9 cells, comparable to the positive control CCCP, indicating mitochondrial dysfunction as part of the cell death mechanism (Fig. 2 J).

3.3. NSCLC SeChry@PURE$_{G4}$-LA$_{24}$ conditioned media (CM) decreases ECs migration and tube-forming capacity

ROS are involved, either directly or indirectly, in the mechanisms underlying physiological, pathophysiological, and over activated angiogenesis [29]. The transendothelial transport of molecules and cells is intricately regulated by vascular ECs [59]. Dysfunction in the regulatory mechanisms of the endothelium and its compromised ability to effectively respond to the physicochemical microenvironment leads to the disruption of endothelial integrity [60]. Changes in the selective permeability barrier of ECs represent early events in oxidative stress-mediated injury, potentially contributing to the extravasation of circulating cancer cells [60]. To clarify if free or encapsulated SeChry could influence angiogenesis, we used HUVECs as an *in vitro* model of human ECs, which were exposed to conditioned media (CM) from NSCLC cells. Wound healing assays were conducted on HUVECs cultured in control conditions and exposed directly to SeChry and SeChry@PURE$_{G4}$-LA$_{24}$, as well as on HUVECs treated with CM from H292 and PC-9 cells cultured in control conditions and previously exposed to SeChry and SeChry@PURE$_{G4}$-LA$_{24}$. We observed a tendency for SeChry to decrease the migration of HUVECs after 6 h, while SeChry@PURE$_{G4}$-LA$_{24}$ significantly reduced HUVEC migration (Fig. 3 A). After 24 h, these treatments exhibited a more pronounced effect, demonstrating significant differences compared to the control. Interestingly, CM from H292 or PC-9 cells exposed to SeChry or SeChry@PURE$_{G4}$-LA$_{24}$ resulted in an even more significant reduction in the migration of HUVECs (Fig. 3 A).

Given that a pro-oxidative microenvironment promotes angiogenesis, we tested the capacity of HUVECs to form vessel-like structures under SeChry or SeChry@PURE$_{G4}$-LA$_{24}$ exposure, using an *in vitro* tube-forming assay. After 6 h, a slight tendency to increase tube-forming capacity was observed with both free and encapsulated SeChry (Fig. 3 B). However, HUVECs exposed to H292 SeChry@PURE$_{G4}$-LA$_{24}$ CM exhibited a significant reduction in branch point density compared to the control. Likewise, HUVECs treated with PC-9 SeChry@PURE$_{G4}$-LA$_{24}$ CM also showed a decrease in vessel-like structures.

We also investigated the impact of SeChry on the adhesion of cancer cells to ECs and their transendothelial migration. In this study, we performed HUVECs co-cultures with H292 and PC-9 cell lines. These cells were placed on top of a HUVECs monolayer previously established. The HUVECs monolayer was exposed to either SeChry or SeChry@PURE$_{G4}$-LA$_{24}$. SeChry demonstrated a tendency to elevate the number of cancer cells adhering to the EC monolayer, with significance observed in PC-9 cell assays (Fig. 3 C). Moreover, both treatments significantly enhanced transendothelial migration in H292 cells, and only SeChry induced a significant increase in PC-9 cells (Fig. 3 D). Thus, SeChry, whether free or encapsulated, exerts diverse effects on EC behavior and cancer cell interactions, highlighting its potential significance in modulating angiogenesis and the TME in NSCLC. In cancer, lactate contributes significantly to angiogenesis by inducing VEGF expression in ECs [61].

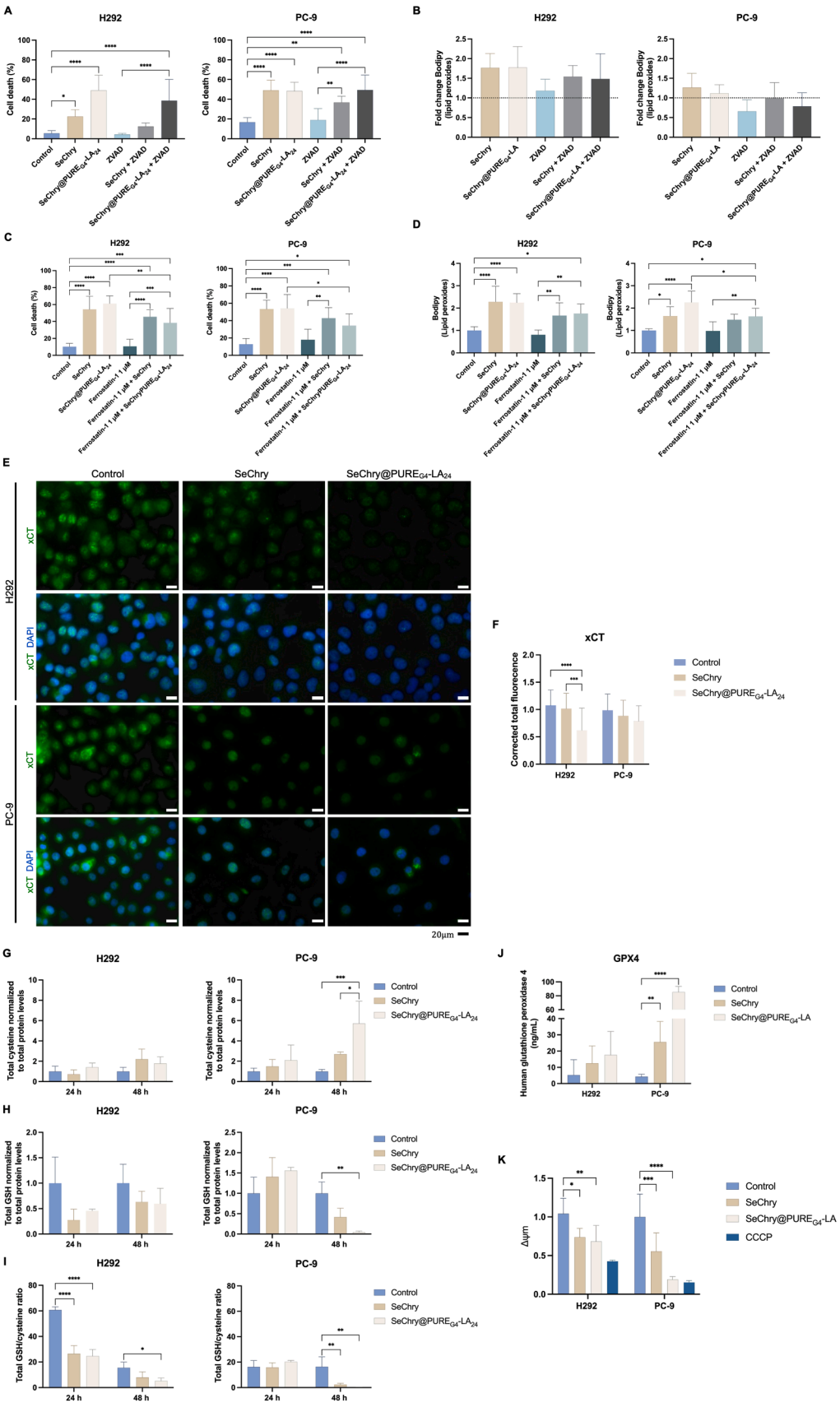

(caption on next page)

Fig. 2. SeChry induces partial caspase-independent cell death associated with lipid peroxidation and disruption of the xCT–GSH–GPX4 axis. Exposure of A549, H292 and PC-9 cells to SeChry/SeChry@PURE$_{G4}$-LA$_{24}$ for 48 h. Percentage of cell death (A) and lipid peroxides (B) in the presence of the apoptosis inhibitor Z-VAD-FMK (50 μM). (C) Percentage of cell death in the presence or absence of the ferroptosis inhibitor Ferrostatin-1 (Fer-1, 1 μM). (D) Lipid peroxide levels following co-treatment with Ferrostatin-1. Immunofluorescence for xCT (E) and quantification of xCT levels (F) by corrected total cell fluorescence (CTCF). High-performance liquid chromatography (HPLC) coupled to fluorescence detection (FLD) was used to measure (G) total cysteine concentration, (H) total glutathione (GSH) concentration, and (I) the ratio between GSH and cysteine was determined in NSCLC cells exposed to SeChry/SeChry@PURE$_{G4}$-LA$_{24}$ for 24 (left) or 48 h (right). (J) Quantitative measurement of glutathione peroxidase 4 (GPX4) protein by ELISA in H292 and PC-9 cells exposed to SeChry/SeChry@PURE$_{G4}$-LA$_{24}$. (K) Assessment of mitochondrial membrane potential (Δψm) using JC-1 staining. Quantification of Δψm is expressed as the red/green fluorescence intensity ratio and normalized to the control condition. CCCP (10 μM) was used as a positive control for Δψm depolarization. Data is represented as mean ± SD. *p < 0.5, **p < 0.01, ***p < 0.001, ****p < 0.0001 (one-way ANOVA or two-way ANOVA with Tukey's multiple comparisons test were used). Data is represented as mean ± SD. *p < 0.5, **p < 0.01, ***p < 0.001, ****p < 0.0001 (one-way ANOVA or two-way ANOVA with Tukey's multiple comparisons test were used).

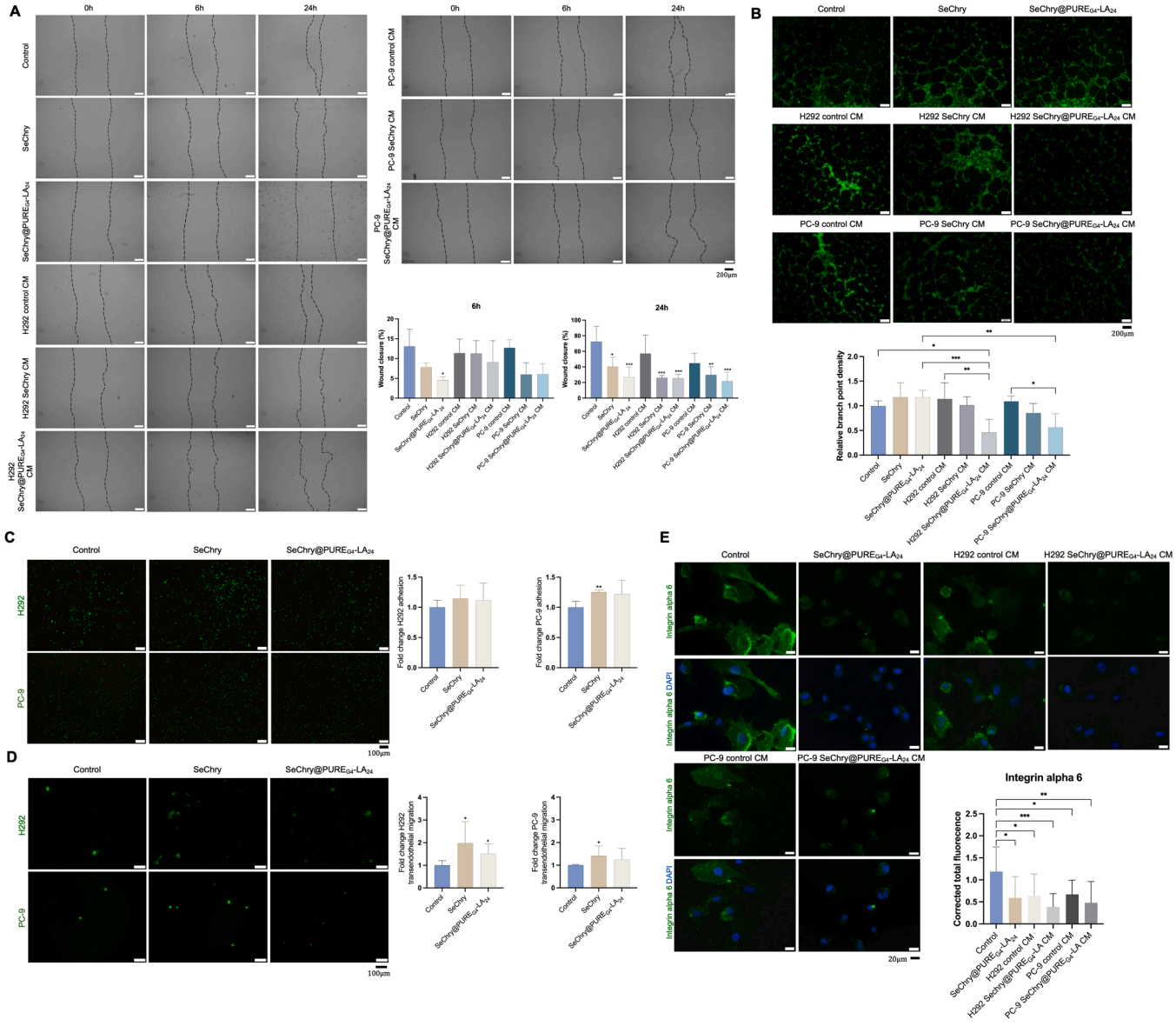

Fig. 3. NSCLC SeChry@PURE$_{G4}$-LA$_{24}$-conditioned media (CM) reduces the migration and tube-forming ability of endothelial cells (ECs). HUVECs were exposed directly to SeChry and SeChry@PURE$_{G4}$-LA$_{24}$, as well as to CM from H292 and PC-9 cells previously exposed to SeChry and SeChry@PURE$_{G4}$-LA$_{24}$. **(A)** Wound healing assay on HUVECs at 0, 6 and 24 h of experimental conditions. **(B)** Branch point density of vessel-like structures in HUVECs after 6 h of experimental conditions. **(C)** NSCLC calcein-labeled cancer cell adhesion on HUVECs and **(D)** transendothelial NSCLC migration. The panels show representative microscope images (scale: 200 or 100 μm; NSCLC-calcein-labeled cells (green). **(E)** Integrin alpha 6 expression profile by immunofluorescence and quantification (CTCF) using *ImageJ*. Data is represented as mean ± SD. *p < 0.5, **p < 0.01, ***p < 0.001, ****p < 0.0001 (one-way ANOVA with Tukey's multiple comparisons test was used).

The release of lactate from tumor cells, facilitated by MCT4, is sufficient to stimulate angiogenesis and support tumor growth [62]. Given the high importance of lactate in the NSCLC TME and the fact that SeChry nanoparticles are functionalized with lactic acid, HUVECs were exposed to lactate or CM from NSCLC treated with lactate for 24 h. The results showed no significant changes in migration capacity, tube-forming ability, NSCLC cell adhesion, or transendothelial migration of NSCLC cells under these conditions (Supplementary Fig. 4). However, there was

a tendency for increased migration and branch point density with the addition of lactate (Supplementary Fig. 4 A). CM from PC-9 cells exposed to lactate similarly demonstrated a tendency to enhance the tube-forming capability of HUVECs (Supplementary Fig. 4B). Furthermore, lactate displayed a propensity to increase adhesion and transendothelial migration of PC-9 cells while showcasing an opposite trend in H292 cells (Supplementary Fig. 4 C). SeChry@PURE$_{G4}$-LA$_{24}$ significantly reduced integrin alpha 6 expression comparing to non-treated HUVECs cells (Fig. 3 E). Conditioned media from H292 control cells and SeChry@PURE$_{G4}$-LA$_{24}$ -treated H292 and PC-9 cells also decreased the expression of this protein.

3.4. SeChry@PURE$_{G4}$-LA$_{24}$ reduces tumor growth and tends to decrease angiogenesis

We evaluated the SeChry@PURE$_{G4}$-LA$_{24}$ anticancer effect *ex vivo* using the CAM assay since we found that NSCLC SeChry@PURE$_{G4}$-LA$_{24}$ CM exhibited the most significant reduction in EC migration and tube-forming capacity. The CAM assay is a cost-effective and efficient alternative for assessing novel drugs and bioactive molecules, as it facilitates quick tumor cell xenografting, tumorigenesis, observation of metastasis and angiogenesis, as well as drug characterization and delivery evaluation [63]. A549 cells showed poor and inconsistent tumor formation in CAM, leading to the selection of H292 and PC9 cells for further studies due to their more reliable tumor-forming ability. Here, H292 cells, representative of the LUSC histological type, and PC-9 cells, representative of the LUAD type, were employed.

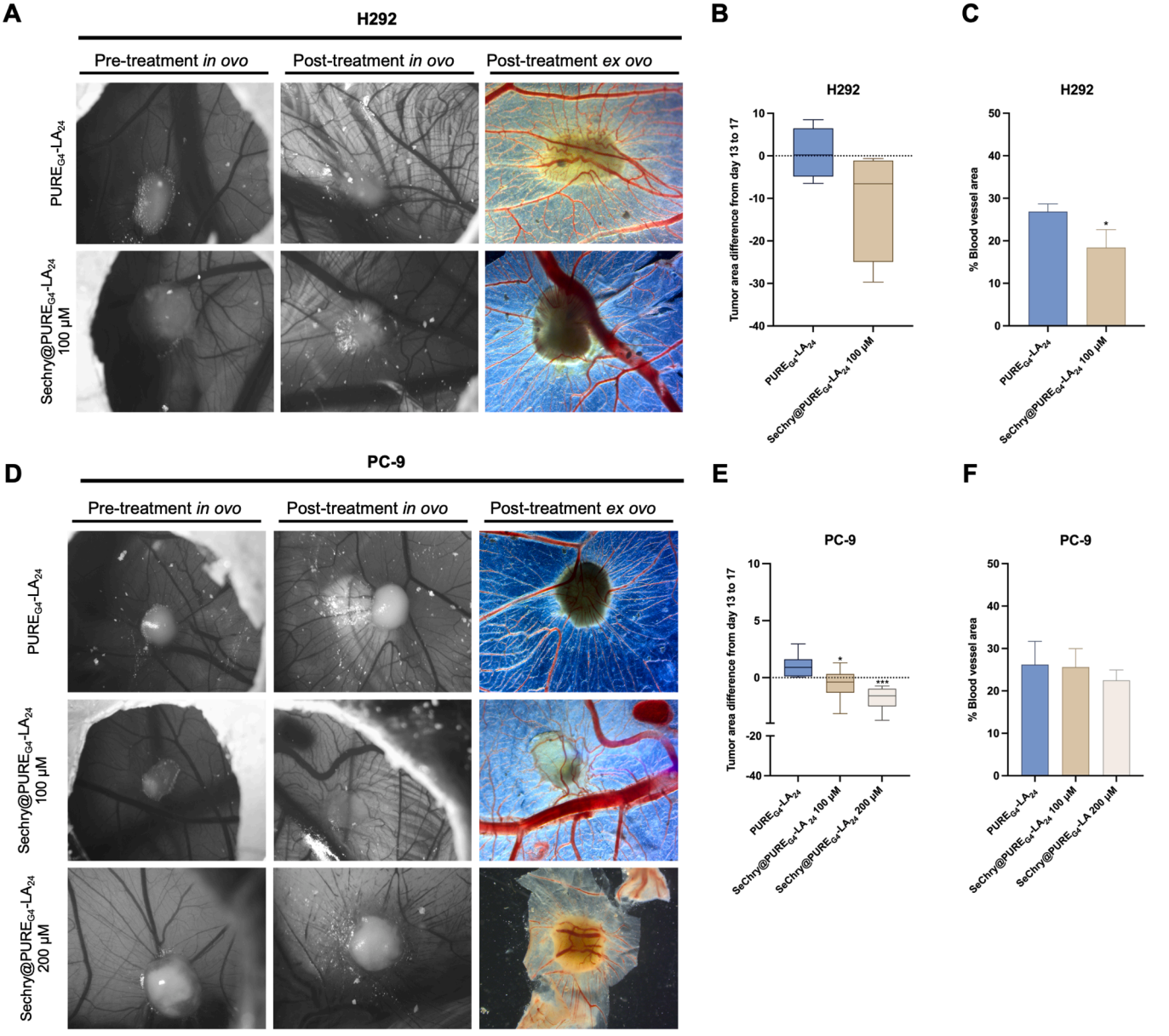

Fig. 4. SeChry@PURE$_{G4}$-LA$_{24}$ reduces tumor growth and angiogenesis. (A) Representative pictures of chicken embryo chorioallantoic membrane (CAM) assay inoculated with H292 cells pre-treatment (day 13) and post-treatment (day 17). CAMs were exposed to PURE$_{G4}$-LA$_{24}$ (control group) and SeChry@PURE$_{G4}$-LA$_{24}$ for 4 days. **(B)** Quantification of H292 tumor area (difference from day 13 to day 17). **(C)** Quantification of the percentage of blood vessel area for the H292 model. **(D)** Representative pictures of CAM inoculated with PC-9 cells pre-treatment and post-treatment. **(E)** Quantification of PC-9 tumor area (difference from day 13 to day 17). **(F)** Quantification of the percentage of blood vessel area for the PC-9 model. Data is represented as mean ± SD. *p < 0.5, **p < 0.01, ***p < 0.001, ****p < 0.0001 (one-way ANOVA with Tukey's multiple comparisons test was used).

Treatment with SeChry@PURE$_{G4}$-LA$_{24}$ (100 μM) showed a trend towards decreased size of H292-derived tumors (Fig. 4 A and B) and a tendency to reduce the percentage of blood vessel area compared to the control empty nanoparticles (PURE$_{G4}$-LA$_{24}$; Fig. 4 C). In PC-9-derived tumors, SeChry@PURE$_{G4}$-LA$_{24}$ significantly decreased the tumor size in a dose-dependent manner (Fig. 4 D and E). However, no significant differences were observed in terms of the percentage of blood vessel area, but the highest concentration of SeChry@PURE$_{G4}$-LA$_{24}$ tended to decrease it (Fig. 4 F).

3.5. SeChry@PURE$_{G4}$-LA$_{24}$ decreases lung tumor burden in NSCLC xenograft mouse models

The next step was to test the *in vivo* efficacy of SeChry@PURE$_{G4}$-LA$_{24}$ in orthotopic xenograft mouse models of NSCLC using H292 and PC-9 cells delivered by tail vein injection. A549 cells failed to form lung tumors in murine models, leading to the selection of H292 and PC9 cells for further studies due to their more reliable tumor-forming ability. After 38 days post-cell injection, the pulmonary administration of the dry powder formulations containing PURE$_{G4}$-LA$_{24}$ (control) or SeChry@-PURE$_{G4}$-LA$_{24}$ nanoparticles was performed four times over the course of one week. Animals were euthanized on day 47 after cell inoculation (2 days after the last administration). H&E staining of lung sections showed that mice treated with SeChry@PURE$_{G4}$-LA$_{24}$ exhibited a significantly reduced tumor burden in the lungs compared to mice exposed to PURE$_{G4}$-LA$_{24}$, the empty nanoformulation (Fig. 5 A and B). When compared to the control group that inhaled PURE$_{G4}$-LA$_{24}$, SeChry@-PURE$_{G4}$-LA$_{24}$ led to a significant decrease in tumor area by 97 % ($p = 0.0092$) in tumors derived from H292 cells and by 83 % ($p = 0.0027$) in tumors derived from PC-9 cells (Fig. 5 B). To gain further insight into cachexia, body weight of the mice was assessed on the day of injection (initial) and the day of euthanasia (final), although weights were measured at least twice per week throughout the study. Mice inoculated with H292 cells, showed a more significant increase in body weight after all administrations of SeChry@PURE$_{G4}$-LA$_{24}$ ($p = 0.0016$ and $p = 0.0003$) compared to mice exposed to PURE$_{G4}$-LA$_{24}$ (Fig. 5 C). In mice injected with PC-9 cells, only the group treated with the SeChry@PURE$_{G4}$-LA$_{24}$ treatment showed a significant ($p = 0.0366$ gain in body weight. These results suggest that mice receiving the control PURE$_{G4}$-LA$_{24}$ treatment exhibited an increased degree of cachexia. Additionally, the treatment caused no morphological changes, necrosis, or fibrosis in the mice's liver and kidneys, indicating no severe systemic toxicity (Fig. 5 D).

We previously showed that SeChry induced significant metabolic changes, particularly in selenocompound metabolism, affecting key pathways such as glycolysis, gluconeogenesis, the tricarboxylic acid (TCA) cycle, and amino acid metabolism in NSCLC cells [35]. To further elucidate these metabolic changes in this context, mice blood sera were evaluated by ^{1}H-NMR spectroscopy. Most differences were observed in the *cpmgpr1d* spectra. Importantly, we did not detect any traces of PURE$_{G4}$-LA$_{24}$ or SeChry@PURE$_{G4}$-LA$_{24}$ in the sera, indicating that the treatment was efficiently delivered to the lungs. Sera collected at euthanasia showed a clear separation of the metabolic profiles between PURE$_{G4}$-LA$_{24}$-treated mice and SeChry@PURE$_{G4}$-LA$_{24}$-treated mice bearing H292 cells (Fig. 5 E). The separation between these groups in mice bearing PC-9 cells is not as evident. Nonetheless, these results indicate that the treatment alters the whole-body metabolic profile. In this context, the metabolic profiles of the mice were further analyzed and revealed that the PURE$_{G4}$-LA$_{24}$ treated mice and the SeChry@-PURE$_{G4}$-LA$_{24}$ treated mice exhibited similar metabolic profiles as indicated by their clustering patterns (Fig. 5 F). The results show that regardless of the cell line from which the tumor originates, mice with a similar tumor burden have comparable metabolic profiles. The analysis of ^{1}H-NMR spectra acquired from the blood sera was performed using buckets comparison with NMRProcFlow 1.4 software and significant buckets were found. Univariate analysis of sera from PURE$_{G4}$-LA$_{24}$ and SeChry@PURE$_{G4}$-LA$_{24}$-treated mice revealed 16 significantly altered buckets in H292 xenografts (Table 1) and 13 significantly altered buckets in PC-9 xenografts (Table 2). The chemical shifts consistent with these metabolites are altered and are depicted in Tables 1 and 2.

Focusing on the altered buckets identified in Tables 1 and 2, unsupervised (PCA) and supervised (PLS-DA) analyses were conducted. These analyses revealed significant metabolic differences between the treatment groups. Both the PCA and PLS-DA plots depicted a clear separation of samples based on their metabolite profiles in the sera from H292 and PC-9 mice xenografts (Fig. 6 A, B, F and G). Cross-validation and permutation tests of the PLS-DA model were performed. The values of R^2 0.89 and 0.9 and Q^2 0.73 and 0.58 for H292 and PC-9 samples respectively revealed satisfactory goodness of fit and goodness of prediction (Supplementary Fig. 5A and B). The nominal P value (0.028) of the permutation test confirmed the validity of the PLS-DA model at a 95 % confidence level (Supplementary Fig. 5C and D). Variable Importance in Projection (VIP) Scores identified the metabolites that contributed most to the group separation in the PLS-DA analysis. The top buckets and corresponding metabolites include B1_9571 (acetate), B2_1353 (glutamine, glutamate, proline), B1_7932 (arginine, lysine) in H292 mice xenografts (Fig. 6 C). Heatmaps were also generated and showed distinct clustering patterns, with most SeChry@PURE$_{G4}$-LA$_{24}$-treated samples exhibiting higher levels of metabolites compared to PURE$_{G4}$-LA$_{24}$, reinforcing the metabolic shifts caused by SeChry@-PURE$_{G4}$-LA$_{24}$ treatment. (Fig. 6 D and I). Acetate was the most important metabolite contributing to the differences observed and was significantly increased in the SeChry@PURE$_{G4}$-LA$_{24}$-treated H292 group (Fig. 6 E). Regarding PC-9 mice xenografts, the top buckets and corresponding metabolites included B2_4602 (glucose), B2_7827 (unknown), and B3_4853 (glucose) (Fig. 6 H). In PC-9 xenografts, altered spectra buckets corresponded to increased glucose, citrate and isobutyrate levels in the SeChry@PURE$_{G4}$-LA$_{24}$-treated animals (Fig. 6J-L). Collectively, these findings suggest that SeChry treatment induces significant metabolic alterations in mice, impacting key metabolites and pathways, particularly those related to energy metabolism and redox homeostasis.

4. Discussion

Tumors often exhibit imbalances in redox equilibrium and disrupted redox signaling, which are pivotal factors contributing to malignant progression and resistance to treatment [10]. The low overall survival rate among NSCLC patients remains a significant challenge in clinical management, emphasizing the critical necessity for innovative therapeutic strategies that can overcome inherent drug resistance [64]. In this study, we assessed the response of NSCLC cell lines representing two histological types (LUAD and LUSC) to SeChry@PURE$_{G4}$-LA$_{24}$ treatment, taking advantage of lactate-enhanced consumption and MCT1 overexpression, to target cysteine metabolism in both *in vitro* and *in vivo* NSCLC models. The observed induction of cell death in all the NSCLC cell lines (Fig. 1), along with the significantly reduced H292- and PC-9-derived tumor burden in the lungs of treated mice (Fig. 5 A and B), highlights SeChry@PURE$_{G4}$-LA$_{24}$ as a valid therapeutic alternative for NSCLC. Cell death induced by SeChry@PURE$_{G4}$-LA$_{24}$ induced cell death in lung cancer cells, seems to be primarily dependent on necrosis or necroptosis (Fig. 1 B). Apoptosis has been identified as a key mechanism for eliminating NSCLC cells when nanoselenium is combined with radiofrequency therapy, accompanied by a simultaneous decrease in the carcinogenesis-related proteins CCND1 and c-Myc [65]. The increased production of ROS and lipid peroxides induced by SeChry@PURE$_{G4}$-LA$_{24}$ (Fig. 1 C and D) highlights its role in triggering oxidative stress. This stress is linked to necrotic/necroptotic cell death, driven by disruptions in cellular energy metabolism, intracellular calcium flux, and further ROS generation [66,67]. In the future, combining a metabolism-targeted therapy capable of inducing necrosis or necroptosis, as SeChry@PURE$_{G4}$-LA$_{24}$, with immunotherapies could be an opportunity to improve the clinical management of NSCLC. Evidence

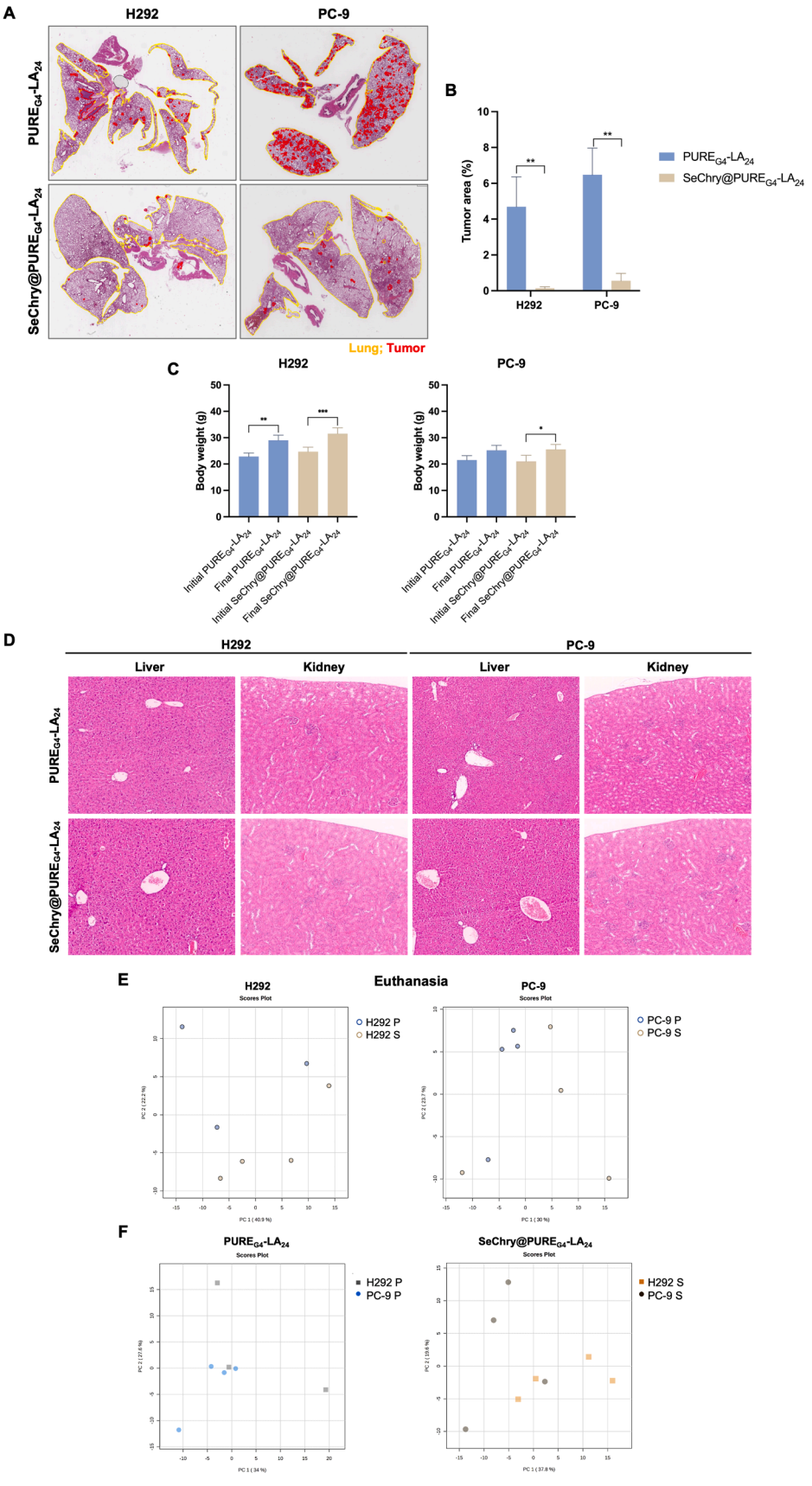

(caption on next page)

Fig. 5. SeChry@PUREG4-LA$_{24}$ reduces lung tumor area in NSCLC xenograft mouse models. H&E from lung sections of mice **(A)** treated with PURE$_{G4}$-LA$_{24}$ (top) and SeChry@PURE$_{G4}$-LA$_{24}$ (bottom) in H292 cells (left) and PC-9 cells (right). Tumor cells are depicted in red, and lungs are depicted in yellow. **(B)** Tumor area percentage was calculated in the H&E from lung sections of mice with QuPath (https://qupath.github.io/). **(C)** Change in mice body weight (g). The body weight of mice was measured on the day of injection (initial) and the day of euthanasia (final). Data is represented as mean ± SD. *p < 0.5, **p < 0.01, ***p < 0.001, ****p < 0.0001 (one-way ANOVA with Tukey's multiple comparisons test was used). **(D)** Representative H&E-stained liver and kidney Section (4 μm) from control, PURE$_{G4}$-LA$_{24}$-, and SeChry@PURE$_{G4}$-LA$_{24}$-treated mice inoculated with H292 cells (left) and PC-9 cells (right). **(E)** Multivariate analysis principal component analysis (PCA) of the ^{1}H-NMR spectra acquired from the blood sera at euthanasia of H292 (left) and PC-9 (right) mice xenografts treated with PURE$_{G4}$-LA$_{24}$ (P) and SeChry@PURE$_{G4}$-LA$_{24}$ (S). **(F)** PCA of the 1H-NMR spectra acquired from the blood sera at euthanasia of PURE$_{G4}$-LA$_{24}$ (left) and SeChry@PURE$_{G4}$-LA$_{24}$ (right) -treated H292 and PC-9 mice xenografts.

Table 1
Altered buckets and probable corresponding metabolites in serum from mice inoculated with H292 cells. Univariate analysis (t test).

Bucket	Probable metabolites	Chemical Shift (ppm)	*t*	*p*	-log10(*p*)	FDR
B1_7748	Arginine, lysine	1.77478	−3.9683	0.010654	1.9725	0.63178
B1_9951	Arginine, lysine	1.9951	−3.7506	0.013285	1.8766	0.63178
B1_7820	Arginine, leucine, lysine	1.7820	−3.6028	0.015498	1.8097	0.63178
B1_9571	Acetate	1.9571	−3.4932	0.017411	1.7592	0.63178
B1_7932	Arginine, lysine	1.7932	−3.4411	0.018413	1.7349	0.63178
B1_7617	Arginine, lysine	1.7617	−3.2274	0.023274	1.6331	0.63178
B3_1412	Unknown	3.1412	3.0741	0.027654	1.5582	0.63178
B2_1249	Glutamine, glutamate, proline	2.1249	−3	0.030098	1.5215	0.63178
B1_8010	Arginine	1.8010	−2.9966	0.030216	1.5198	0.63178
B4_3282	Threonine	4.3282	2.9543	0.031726	1.4986	0.63178
B2_1353	Glutamine, glutamate, proline	2.1353	−2.9542	0.031731	1.4985	0.63178
B2_1415	Glutamine, glutamate, proline	2.1415	−2.8978	0.033876	1.4701	0.63178
B4_3210	Threonine	4.3210	2.8849	0.034389	1.4636	0.63178
B1_9453	Arginine. lysine	1.9453	−2.8615	0.035344	1.4517	0.63178
B2_1292	Glutamine, glutamate, proline	2.1292	−2.8187	0.037164	1.4299	0.63178
B1_7536	Arginine, lysine	1.7536	−2.5941	0.048596	1.3134	0.66336

Table 2
Altered buckets and probable corresponding metabolites in serum from mice inoculated with PC-9 cells. Univariate analysis (t test).

Bucket	Probable metabolites	Chemical Shift (ppm)	*t*	*p*	-log10(*p*)	FDR
B3_3323	Glucose	3.3323	−4.9477	0.0025839	2.5877	0.41184
B2_6956	Citrate	2.6956	−4.5712	0.0038057	2.4196	0.41184
B2_6706	Methionine	2.6706	−4.2174	0.0055773	2.2536	0.41184
B3_4602	Glucose	3.4602	−3.8947	0.008033	2.0951	0.41184
B2_7087	Citrate	2.7087	−3.8902	0.0080753	2.0928	0.41184
B3_4853	Glucose	3.4853	−3.3329	0.01575	1.8027	0.54406
B2_3630	Isobutyrate	2.3630	−3.2093	0.018384	1.7356	0.54406
B1_1014	Isobutyrate	1.1014	−3.1998	0.018604	1.7304	0.54406
B2_7827	Unknown	2.7827	3.1748	0.019202	1.7167	0.54406
B2_6852	Citrate	2.6852	−3.0796	0.021673	1.6641	0.55266
B1_0703	Valine	1.0702	−2.8548	0.028999	1.5376	0.67224
B1_1176	Isobutyrate	1.1176	−2.712	0.035014	1.4558	0.70692
B1_0869	Valine	1.0869	−2.6903	0.036039	1.4432	0.70692

suggests that necrosis robustly activates the immune system, promoting the targeting and clearance of cellular debris from dying cells [68]. Additionally, a study exploring the molecular mechanisms behind therapy-induced necrosis identified TRPM4 - a calcium-activated, ATP-inhibited, sodium-selective plasma membrane channel - as a key mediator of both cell death and immune activation following various necrosis-inducing anticancer treatments [69]. Therefore, therapies inducing necrosis or necroptosis may improve immunotherapies for solid tumors and challenging cancers.

SeChry@PURE$_{G4}$-LA$_{24}$ compared to free SeChry, led to a significant increase in ROS in A549 and PC-9 cells (Fig. 1 C). Contrarily, H292 cells exhibited a reduction in ROS levels, and notably, free SeChry caused an elevation in mitochondrial ROS exclusively in H292 cells (Supplementary Fig. 3). These findings align with previous reports linking SeChry cytotoxicity to alterations in mitochondrial membrane potential, indicative of increased oxidative stress [70]. Cellular membranes are prone to damage from ROS due to their high levels of PUFAs, a process commonly referred to as lipid peroxidation [71-73]. Ferroptosis was initially characterized as an iron-dependent programmed cell death marked by the accumulation of lipid peroxides dependent on iron-related free radicals, such as ROS [74]. Lipid peroxide levels were significantly increased by SeChry@PURE$_{G4}$-LA$_{24}$ in all cell lines (Fig. 1 D) and rescued by ferrostatin-1 (Fig. 2D), reinforcing the involvement of ferroptosis in SeChry's mechanism of action. Lipid peroxidation is regulated by cellular GSH levels, which are controlled by the *SLC7A11*/xCT transporter and the GPX4 enzyme [75]. xCT imports cystine, which is converted to cysteine for GSH synthesis by the enzymes GCLC and GSS [76]. GSH then reduces oxidative stress through GPX4 activity [77]. Inhibiting xCT or GPX4 decreases antioxidant defenses, leading to ROS buildup, lipid peroxidation, and ferroptosis [75]. Based on this, we investigated whether SeChry and SeChry@PUREG4-LA$_{24}$ affect this redox regulatory pathway in NSCLC cells.

Strong evidence for the involvement of ferroptosis in the cytotoxic effects of SeChry and SeChry@PURE$_{G4}$-LA$_{24}$ was suggested by the reduced xCT expression upon SeChry@PURE$_{G4}$-LA$_{24}$ (Fig. 2 C and D). Although cysteine levels remained stable or slightly increased in both cell lines (Fig. 2E), the GSH/cysteine ratio was significantly reduced, particularly in H292 cells treated with SeChry and in PC-9 cells treated with SeChry@PURE$_{G4}$-LA$_{24}$ (Fig. 2 G). This implies that GSH depletion results from impaired synthesis or increased oxidative consumption,

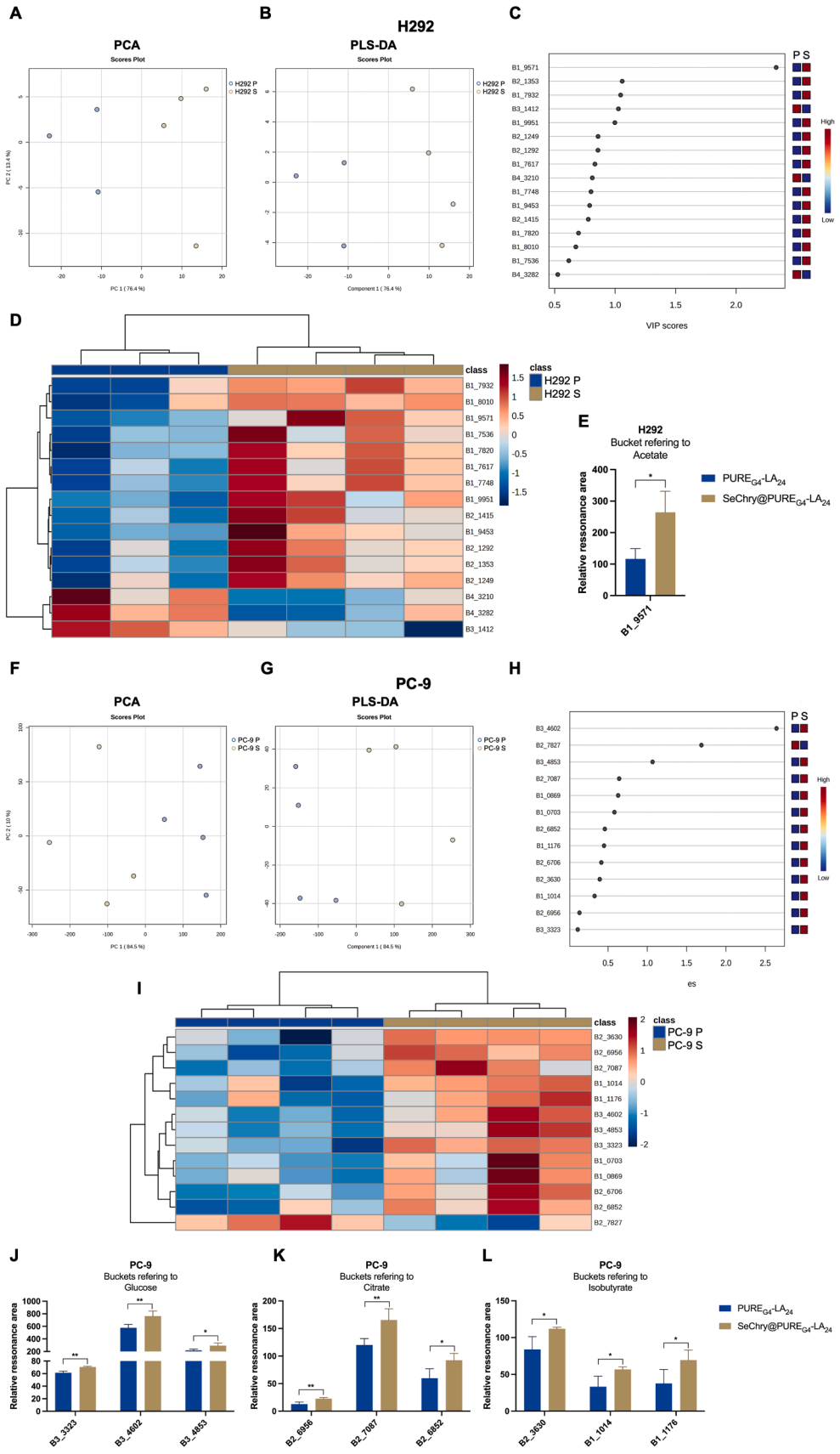

(caption on next page)

Fig. 6. SeChry@PURE$_{G4}$-LA$_{24}$ induces significant metabolic shifts in the sera of H292 and PC-9 mice xenografts. (A) PCA and **(B)** Partial Least-Squares Discriminant Analysis (PLS-DA) of the ^{1}H-NMR spectra acquired from the blood sera at euthanasia of H292 mice xenografts treated with PURE$_{G4}$-LA$_{24}$ (P) and SeChry@PURE$_{G4}$-LA$_{24}$ (S), considering only significantly altered buckets. **(C)** Variable of Importance (VIP) scores plots depicting the 15 most significant buckets (VIP > 1.0) contributing to the group separations observed in the PLS-DA model in H292 xenografts. **(D)** Heatmap of the 15 significantly altered buckets in H292 xenografts. **(E)** Relative resonance area of the bucket corresponding to acetate, allowing the separation between PURE$_{G4}$-LA$_{24}$ and SeChry@PURE$_{G4}$-LA$_{24}$ group in H292 xenografts. **(F)** PCA and **(G)** PLS-DA of the ^{1}H-NMR spectra acquired from the blood sera at euthanasia of PC-9 mice xenografts treated with PURE$_{G4}$-LA$_{24}$ (P) and SeChry@PURE$_{G4}$-LA$_{24}$ (S), considering only significantly altered buckets. **(H)** Variable of Importance (VIP) score plots depicting the 13 most significant buckets (VIP > 1.0) contributing to the group separations observed in the PLS-DA model in PC-9 xenografts. **(I)** Heatmap of the 13 significantly altered buckets in PC-9 xenografts. **(J-L)** Relative resonance area of the buckets corresponding to the metabolites that allow the separation between PURE$_{G4}$-LA$_{24}$ and SeChry@PURE$_{G4}$-LA$_{24}$ group in PC-9 xenografts. Data is represented as mean ± SD. *p < 0.5, **p < 0.01, ***p < 0.001, ****p < 0.0001 (two-tailed unpaired Student's *t*-test was used).

rather than limited precursor availability. These findings align with our prior work showing that SeChry inhibits CBS, a key enzyme in the transsulfuration pathway and cysteine degradation [50], which further contributes to reduced GSH biosynthesis. The PTGS2 expression, a downstream marker associated with lipid peroxidation and ferroptosis, was upregulated in H292 and PC-9 cells exposed to free SeChry and in H292 cells exposed to SeChry@PURE$_{G4}$-LA$_{24}$ (Fig. 1 E), supporting ferroptosis. While PTGS2's mechanistic role in ferroptosis is not fully understood [78,79], its induction has been widely used as a marker of ferroptotic stress, and its regulation by NRF2 and GPX4 loss supports its relevance in this context [32,80,81]. In PC-9 cells treated with SeChry@PURE$_{G4}$-LA$_{24}$, GPX4 mRNA levels were reduced (Fig. 1 E), whereas GPX4 protein levels were increased in H292 and PC-9 cells treated with both free and encapsulated SeChry (Fig. 2 H). This suggests a compensatory response to increased lipid peroxidation; however, given the observed GSH depletion, the functionality of GPX4 is likely compromised, reducing its scavenging effect. Moreover, GSS mRNA levels were significantly downregulated by SeChry@PURE$_{G4}$-LA$_{24}$ in PC-9 cells (Fig. 1 E), showing that GSH biosynthesis is compromised in this cell line. Together, these findings demonstrate that SeChry and SeChry@PURE$_{G4}$-LA$_{24}$ disrupt the cystine–cysteine–GSH–GPX4 axis, promoting ferroptotic cell death through redox imbalance and antioxidant system failure. The loss of $\Delta\psi m$ observed upon SeChry and SeChry@PURE$_{G4}$-LA$_{24}$ (Fig. 2 K), may indicate early mitochondrial destabilization, which can enhance ROS production and lipid peroxidation, thereby amplifying ferroptotic cell death [82]. Iron overload induces mitochondrial dysfunction, as demonstrated by impaired mitochondrial respiration, elevated mitochondrial ROS levels, mitochondrial swelling, and notably, depolarization of the mitochondrial membrane potential, a key feature of the ferroptosis phenotype [83,84]. These results support the induction of ferroptosis as a mechanism of action of Sechry, which is further potentiated by its targeted delivery through SeChry@PURE$_{G4}$-LA$_{24}$ (Fig. 2 K).

Cancer is a complex disease where the TME, consisting of cellular (fibroblasts, adipocytes, endothelial, and immune cells) and non-cellular elements (growth factors, chemokines, cytokines, proteases, extracellular matrix), collectively support cancer cell survival and contributes to cancer progression [85,86]. In the development of lung cancer, the early recruitment of new blood vessels, where ECs play a crucial role, is a significant event [85]. Blood vessels are essential in the TME for supplying nutrients and oxygen to the tumor [85]. In the TME, stressful conditions such as hypoxia and metabolite availability tend to support pro-angiogenic events [87]. In this study, it was demonstrated that HUVECs directly exposed to free or encapsulated SeChry showed significantly reduced migration compared to control HUVECs (Fig. 3 A). Additionally, lactate, known to promote angiogenesis [61], was shown to increase migration and branch point density in HUVECs (Supplementary Fig. 4 A). Interestingly, CM from H292 or PC-9 cells exposed to SeChry or SeChry@PURE$_{G4}$-LA$_{24}$ led to an even greater reduction in HUVECs migration. This aligns with previously reported decreased levels of lactate in NSCLC cells' CM following SeChry treatment [35], which likely contributes to the impaired HUVECs migration. On the other hand, both free and encapsulated SeChry tended to increase the tube-forming capacity of HUVECs (Fig. 3 B) and the adherence of NSCLC to the HUVECs monolayer needed for transendothelial migration (Fig. 3 C and D). Our previous study showed that xCT inhibition with erastin induced a ferroptosis-like mechanism in HUVECs, leading to increased branch point density, enhanced cancer cell adhesion, and stimulated transendothelial migration [27]. Therefore, SeChry appears to interfere with xCT function and, consequently, with cysteine uptake, potentially contributing to the activation of this pro-angiogenic ferroptotic mechanism. HUVECs treated with CM from NSCLC cells exposed to SeChry@PURE$_{G4}$-LA$_{24}$ showed reduced branch point density and vessel-like structures (Fig. 3 B), indicating that SeChry-treated cancer cells release pro-oxidant factors that inhibit endothelial cell migration and tube formation, thus suppressing angiogenesis. This was supported by *ex vivo* CAM assays, where SeChry@PURE$_{G4}$-LA$_{24}$ reduced tumor growth and tended to decrease angiogenesis (Fig. 4). Although the highest concentration tested resulted in egg mortality, the overall findings suggest SeChry exerts anti-cancer effects both by inducing cancer cell death and by impairing angiogenesis through cancer cell-mediated mechanisms. A recent study showed that chrysin reduced HIF-1α expression in tumor cells *in vitro* and hindered tumor cell-induced angiogenesis *in vivo* [88]. Additionally, selenium was shown to exert a significant inhibitory effect on tumor angiogenesis by targeting TrxR, leading to cell apoptosis and cell cycle arrest, and increasing reactive ROS production in ECs [89].

The innovative outcome of this study is the significantly reduced lung tumor burden by the pulmonary administration of the dry powder formulations containing SeChry@PURE$_{G4}$-LA$_{24}$. Moreover, mice receiving this therapy showed less cachexia than those exposed to the empty nanoparticles PURE$_{G4}$-LA$_{24}$ (Fig. 5 A, B and C), highlighting the reduced disease progression in the treated group. We previously reported that SeChry disrupts cysteine metabolism and depletes GSH, leading to cell death [56]. Additionally, SeChry can degrade intracellularly, releasing selenium and chrysin, both of which have demonstrated anti-cancer effects in various studies across different cancer models [90-92]. The inhalable drug delivery system presented in our study provides a non-invasive method for targeting cancer cells in the lungs. Inhalation approaches can minimize systemic toxicities affecting the whole body and allow for lower doses while enhancing local drug concentration and improving anti-tumor therapy [93]. Importantly, no morphological alterations, including necrosis or fibrosis, were observed in the liver and kidneys of the mice, the primary organs responsible for drug excretion, indicating that the treatment did not cause severe systemic toxic effects by the end of the experimental protocol (Fig. 5 D). This aligns with the advantage of pulmonary delivery systems, which, compared to conventional oral or intravenous routes, benefit from lower enzyme activity in the lungs, thereby reducing hepatic metabolism and enhancing drug bioavailability [93,94]. The reduced activation of angiogenesis following treatment may contribute to the absence of detectable SeChry in the bloodstream of treated mice. This supports the effectiveness of direct tumor-site delivery, which minimizes exposure to other organs, reduces toxicity to healthy tissues, and promotes a rapid therapeutic response [95]. Previous studies have demonstrated the promise of dendrimer-based delivery systems for lung-targeted therapies. For example, DOX-conjugated dendrimers significantly increased drug retention in the lungs and enhanced anti-tumor efficacy compared

to conventional doxorubicin administration [96]. Additionally, siRNA-loaded PAMAM dendriplexes successfully targeted lung epithelial cells, leading to effective gene silencing and potential therapeutic benefits [97]. Nevertheless, the functionalization of nanoparticles with lactate is innovative, and although comparable studies are lacking, it appears to enhance the specific delivery of nanoparticles and SeChry to cancer cells. In solid tumors, the enhanced permeability and retention (EPR) effect occurs due to the leakiness of blood vessels and impaired lymphatic drainage, allowing nanoparticles to extravasate from the bloodstream and accumulate in the TME [98]. The EPR effect and passive accumulation of nanoparticles in the TME, driven by pressure gradients, are insufficient to fully explain nanoparticle entry into cancer cells. Therefore, active mechanisms of cellular entry, retention, and clearance must also be involved, as reviewed elsewhere [100,98,99].

Another issue that warrants further clarification is the mechanism mediating the uptake of SeChry@PURE$_{G4}$-LA$_{24}$ directly by cancer cells. Extensive research has shown that nanoparticles carrying drugs can evade efflux transporters by entering cancer cells through endocytic pathways rather than passive diffusion. This allows the drug to be released closer to the nucleus, away from the cell membrane where efflux pumps are concentrated [101]. Ligand-functionalized nanoparticles can trigger receptor-mediated endocytosis, enabling efficient internalization and drug delivery [102]. Common uptake routes include clathrin-mediated and caveolae-mediated endocytosis, as well as macropinocytosis [103]. The efficiency of these processes is strongly influenced by the nanoparticle's physicochemical properties, such as size, shape, charge, and lipophilicity, as well as the type of target cell [104]. Cancer cells express significantly higher levels of MCTs compared to normal cells; therefore, lactate-functionalized nanoparticles can enhance the EPR effect as well as mediate endocytosis. The activation of bulk or caveolae-mediated endocytosis by MCT1 has been described [105,106], which may favor the specificity of targeting cancer cells with SeChry@PURE$_{G4}$-LA$_{24}$. In colon cancer cells, it was demonstrated that polyethylene glycol (PEG) nanoparticles functionalized with butyrate are efficiently imported by MCT1-mediated endocytosis [107]. In a similar system using folate-functionalized PURE to take advantage of the increased expression of folate receptor-alpha (FR-α) in cancer cells, we demonstrated nanoparticle internalization by employing fluorescein-loaded PURE$_{G4}$-FA$_2$ (FL@PURE$_{G4}$-FA$_2$). We observed that as the nanoparticle concentration increased, the intracellular fluorescein signal also increased, with uptake proportional to the levels of FR-α expression [108].

Treatment with SeChry@PURE$_{G4}$-LA$_{24}$-induced systemic metabolic changes, as reflected by altered serum metabolite profiles (Fig. 5 E). In H292 xenografts, increased acetate (Fig. 6 E) and citrate (Fig. 6 K) levels suggest mitochondrial dysfunction and impaired TCA cycle activity [109]. Elevated glucose levels (Fig. 6 J) in treated mice may result from reduced cellular glucose uptake, enhanced gluconeogenesis, or hormonal imbalances affecting glucose regulation [110]. In PC-9 xenografts, increased isobutyrate levels (Fig. 6 L) suggest enhanced branched-chain amino acid (BCAA) catabolism [111], possibly reflecting metabolic stress or a shift toward alternative energy sources. As short-chain fatty acids (SCFAs), including isobutyrate, play roles in cellular energy production, signaling, and maintaining metabolic homeostasis [112], these changes collectively point to disrupted energy metabolism and cellular stress responses. In Fig. 7, we illustrate how the disruption of energy metabolism and redox homeostasis lead to cancer cell death, highlighting the therapeutic potential of SeChry@PURE$_{G4}$-LA$_{24}$ in NSCLC treatment.

A major outcome of this study is the development of an inhalable nanoformulation designed for the localized delivery of the therapeutic agent directly to lung cancer cells, thereby circumventing the need for administration via the bloodstream. The SeChry@PURE$_{G4}$-LA$_{24}$ targeted delivery strategy enhances therapeutic efficacy, as evidenced by the significantly reduced tumor burden in the lungs. This is achieved by maximizing drug concentration at the tumor site while minimizing off-target distribution to healthy tissues. Additionally, the identification of altered serum metabolites suggests their potential as non-invasive biomarkers for following the therapeutic efficacy of SeChry@PURE$_{G4}$-LA$_{24}$ in NSCLC treatment. Monitoring such biomarkers in real time may facilitate early prediction of treatment outcomes, allowing for timely adjustments to dosage or regimen to enhance efficacy and reduce toxicity. This underscores the clinical relevance of metabolite profiling in optimizing SeChry-based therapies and improving patient management and personalized therapeutic strategies.

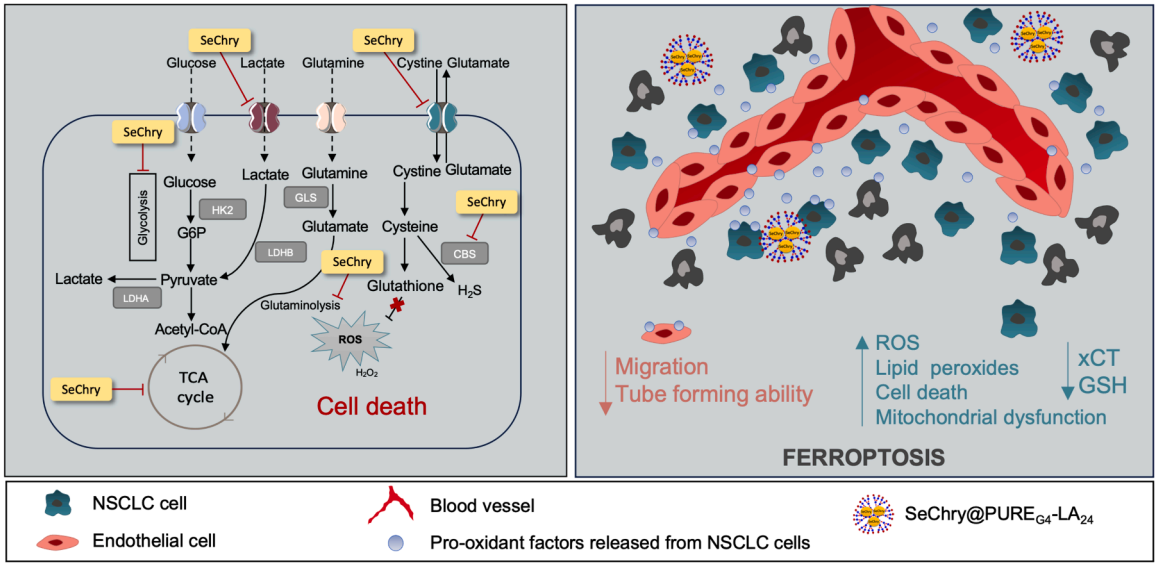

Fig. 7. SeChry and SeChry@PURE$_{G4}$-LA$_{24}$ disrupt NSCLC cell metabolism, increasing oxidative stress and promoting cell death. SeChry treatment induces disruptions in redox homeostasis and cellular biosynthesis, affecting glucose, lactate, glutamine, cystine, and glutamate metabolism. SeChry@PURE$_{G4}$-LA$_{24}$ induces high levels of ROS and lipid peroxides, leading to mitochondrial dysfunction and promoting oxidative stress and cell death through ferroptosis. The treatment impacts the xCT-GSH axis, contributing to redox imbalance. NSCLC cells exposed to SeChry@PURE$_{G4}$-LA$_{24}$ release pro-oxidant factors that decrease the migration and tube-forming ability of endothelial cells, while also exhibiting disrupted pyruvate metabolism and altered glutaminolysis pathways.

Declarations

Ethical Approval

The project was approved by the NOVA Medical School Ethical Committee (Ref: 75/2020/CEFCM).

CRediT author statement

CM - wrote the 1st draft of the paper, planned and performed the majority of the experiments, revised and discussed the paper; FM- performed NMR analysis, revised and discussed the paper; SG- performed CAM experiments, revised and discussed the paper; JG- performed HPLC experiments, revised and discussed the paper; HB- optimized the synthesis of SeChry@PURE$_{G4}$-LA$_{24}$ and confirmed the chemical structure, revised and discussed the paper; TC and AA-R- performed the inhalator formulation, revised and discussed the paper; FS- performed organs processing, revised and discussed the paper; BA- performed in vitro experiments, revised and discussed the paper; MC and SA- performed pathology analysis, revised and discussed the paper; FA- coordinated CAM assays, revised and discussed the paper; SAP- coordinated HPLC analysis, revised and discussed the paper; HM and MMG- performed and coordinate the murine models, revised and discussed the paper; LGG- coordinated NMR spectroscopy analysis, revised and discussed the paper; VDBB- coordinated the drug/nanoparticles synthesis and respective nanoformulations, revised and discussed the paper; JS- coordinated and supervised whole the project, responsible for getting funding, revised and discussed the paper.

Supplementary Figure 1 - Determination of SeChry and SeChry@PURE$_{G4}$-LA$_{24}$ EC50 for HUVECs. The effective concentration 50 (EC$_{50}$) was determined based on the cell death levels induced by different concentrations of selenium-chrysin (SeChry) **(A)** and encapsulated SeChry@PURE$_{G4}$-LA$_{24}$ **(B)**. Cell death was determined by flow cytometry, measuring Annexin V-FITC and propidium iodide (PI) levels.

Funding

The institutions are funded by Fundação para a Ciência e a Tecnologia/Ministério da Ciência, Tecnologia e Ensino Superior (FCT/MCTES, Portugal) through national funds to iNO-VA4Health (UIDB/04462/2020 and UIDP/04462/2020), to MOSTMICRO-ITQB (UIDB/04612/2020 and UIDP/04612/2020) and the Associated Laboratory LS4FUTURE (LA/P/0087/2020). During the course of PhD, Cindy Mendes was funded by Liga Portuguesa Contra o Cancro –Nucleo regional Sul (LPCC-NRS) and by an FCT individual Ph.D. fellowship (2020.06956.BD). Isabel Lemos was funded by an FCT individual Ph.D. fellowship (UI/BD/154203/2022). Ana Hipólito was funded by a FCT individual Ph.D. fellowship (SFRH/BD/148441/2019). Filipa Martins was funded by a FCT individual Ph.D. fellowship (2020.04780.BD). Luis G. Gonçalves was financed by a FCT contract according to DL57/2016, [SFRH/BPD/111100/2015]. This work benefited from access to CERMAX, ITQB-NOVA, Oeiras, Portugal with equipment funded by FCT, project AAC 01/SAICT/2016.

CRediT authorship contribution statement

Bruna Abreu: Writing – review & editing, Methodology, Investigation, Formal analysis. **Miguel Cristovão:** Writing – review & editing, Methodology, Investigation. **Saudade André:** Writing – review & editing, Validation, Methodology, Investigation, Formal analysis. **Cindy Mendes:** Writing – review & editing, Writing – original draft, Validation, Methodology, Investigation, Formal analysis, Data curation, Conceptualization. **Pereira Sofia A:** Writing – review & editing, Supervision, Methodology, Investigation, Formal analysis, Conceptualization. **Filipa Martins:** Writing – review & editing, Methodology, Investigation, Formal analysis. **Fátima Baltazar:** Writing – review & editing, Supervision, Investigation, Conceptualization. **Sara Granja:** Writing – review & editing, Methodology, Investigation, Conceptualization. **Marques Helena:** Writing – review & editing, Supervision, Investigation, Conceptualization. **Joana Gonçalves:** Writing – review & editing, Methodology, Investigation, Formal analysis. **Gaspar Manuela:** Writing – review & editing, Supervision, Methodology, Investigation, Formal analysis. **Barros Helio:** Writing – review & editing, Methodology, Investigation. **Gonçalves Luis:** Writing – review & editing, Validation, Supervision, Methodology, Investigation, Formal analysis, Data curation, Conceptualization. **Teresa Casimiro:** Writing – review & editing, Methodology, Investigation, Conceptualization. **Bonifácio Vasco:** Writing – review & editing, Supervision, Methodology, Investigation, Conceptualization. **Ana Aguiar-Ricardo:** Writing – review & editing, Methodology. **Jacinta Serpa:** Writing – review & editing, Writing – original draft, Validation, Supervision, Project administration, Funding acquisition, Formal analysis, Data curation, Conceptualization. **Fernanda Silva:** Writing – review & editing, Methodology, Investigation.

Declaration of Competing Interest

The authors declare that they have no known competing financial interests or personal relationships that could have appeared to influence the work reported in this paper.

Appendix A. Supporting information

Supplementary data associated with this article can be found in the online version at doi:10.1016/j.biopha.2025.118405.

Data availability

Data will be made available on request.

References

[1] R.L. Siegel, K.D. Miller, H.E. Fuchs, A. Jemal, Cancer statistics, 2022, CA Cancer J. Clin. 72 (2022) 7–33, https://doi.org/10.3322/CAAC.21708.
[2] M.A. Bareschino, C. Schettino, A. Rossi, et al., Treatment of advanced non small cell lung cancer, J. Thorac. Dis. 3 (2011) 122–133, https://doi.org/10.3978/J.ISSN.2072-1439.2010.12.08.
[3] H. Lemjabbar-Alaoui, O.U.I. Hassan, Y.-W. Yang, P. Buchanan, Lung cancer: biology and treatment options, Biochim Biophys. Acta 1856 (2015) 189–210, https://doi.org/10.1016/j.bbcan.2015.08.002.
[4] N. Wathoni, L.E. Puluhulawa, I.M. Joni, et al., Monoclonal antibody as a targeting mediator for nanoparticle targeted delivery system for lung cancer, Drug Deliv. 29 (2022) 2959–2970, https://doi.org/10.1080/10717544.2022.2120566.
[5] L.N. Mathieu, E. Larkins, A.K. Sinha, et al., FDA approval summary: atezolizumab as adjuvant treatment following surgical resection and Platinum-Based chemotherapy for stage II to IIIA NSCLC, Clin. Cancer Res 29 (2023) 2973–2978, https://doi.org/10.1158/1078-0432.CCR-22-3699.
[6] F. Cortiula, B. Reymen, S. Peters, et al., Immunotherapy in unresectable stage III non-small-cell lung cancer: state of the art and novel therapeutic approaches, Ann. Oncol. 33 (2022) 893–908, https://doi.org/10.1016/j.annonc.2022.06.013.
[7] X. Zhu, Z. Yu, L. Feng, et al., Chitosan-based nanoparticle co-delivery of docetaxel and curcumin ameliorates anti-tumor chemoimmunotherapy in lung cancer, Carbohydr. Polym. 268 (2021) 1–14, https://doi.org/10.1016/j.carbpol.2021.118237.
[8] B.L. Horton, D.M. Morgan, N. Momin, et al., Lack of CD8+T cell effector differentiation during priming mediates checkpoint blockade resistance in non-small cell lung cancer, Sci. Immunol. 6 (2021) eabi8800, https://doi.org/10.1126/sciimmunol.abi8800.
[9] E.K. Singhi, F. Mott, M. Worst, et al., Clinical outcomes of immunotherapy continued beyond radiographic disease progression in older adult patients with advanced non-small cell lung cancer, Oncol. Lett. 25 (2023) 262, https://doi.org/10.3892/OL.2023.13848.
[10] F. Xing, Q. Hu, Y. Qin, et al., The relationship of redox with hallmarks of cancer: the importance of homeostasis and context, Front Oncol. 12 (2022) 862743, https://doi.org/10.3389/fonc.2022.862743.
[11] G.Y. Liou, P. Storz, Reactive oxygen species in cancer, Free Radic. Res 44 (2010) 479–496, https://doi.org/10.3109/10715761003667554.
[12] P. Gao, I. Tchernyshyov, T.C. Chang, et al., c-Myc suppression of miR-23a/b enhances mitochondrial glutaminase expression and glutamine metabolism, 458, Nature 2009 458 (7239) (2009) 762–765, https://doi.org/10.1038/nature07823.

[13] D. Anastasiou, G. Poulogiannis, J.M. Asara, et al., Inhibition of pyruvate kinase M2 by reactive oxygen species contributes to cellular antioxidant responses, Science 334 (2011) 1278–1283, https://doi.org/10.1126/science.1211485.

[14] Z. Liao, D. Chua, N.S. Tan, Reactive oxygen species: a volatile driver of field cancerization and metastasis, Mol. Cancer 18 (2019) 1–10, https://doi.org/10.1186/s12943-019-0961-y.

[15] E. Panieri, M.M. Santoro, ROS homeostasis and metabolism: a dangerous liason in cancer cells, 7:6 7:e2253–e2253, Cell Death Dis. 2016 (2016), https://doi.org/10.1038/cddis.2016.105.

[16] R. Huang, H. Chen, J. Liang, et al., Dual role of reactive oxygen species and their application in cancer therapy, J. Cancer 12 (2021) 5543–5561, https://doi.org/10.7150/JCA.54699.

[17] N. Reymond, B.B. D'Água, A.J. Ridley, Crossing the endothelial barrier during metastasis, Nat. Rev. Cancer 13 (2013) 858–870, https://doi.org/10.1038/NRC3628.

[18] S. Reuter, S.C. Gupta, M.M. Chaturvedi, B.B. Aggarwal, Oxidative stress, inflammation, and cancer: how are they linked? Free Radic. Biol. Med 49 (2010) 1603–1616, https://doi.org/10.1016/j.freeradbiomed.2010.09.006.

[19] P. Storz, Reactive oxygen species in tumor progression, Front Biosci. 10 (2005) 1881–1896, https://doi.org/10.2741/1667.

[20] T.H. Adair, J.-P. Montani, Angiogenesis. In: colloquium series on integrated systems physiology: from molecule to function to disease, Morgan Claypool Life Sci. (2010).

[21] N. Nishida, H. Yano, T. Nishida, et al., Angiogenesis in cancer, Vasc. Health Risk Manag 2 (2006) 213–219, https://doi.org/10.2147/vhrm.2006.2.3.213.

[22] M. Rajabi, S.A. Mousa, The role of angiogenesis in cancer treatment, Biomedicines 5 (2017) 34, https://doi.org/10.3390/biomedicines5020034.

[23] S. Arfin, N.K. Jha, S.K. Jha, et al., Oxidative stress in cancer cell metabolism, Antioxidants 10 (2021) 642, https://doi.org/10.3390/antiox10050642.

[24] T. Matsumoto, L. Claesson-Welsh, VEGF receptor signal transduction, Sci. STKE 2001 (2001) 1–17, https://doi.org/10.1126/stke.2001.112.re21.

[25] N. Ferrara, T. Davis-Smyth, The biology of vascular endothelial growth factor, Endocr. Rev. 18 (1997) 4–25, https://doi.org/10.1210/edrv.18.1.0287.

[26] M. Ushio-Fukai, Y. Nakamura, Reactive oxygen species and angiogenesis: NADPH oxidase as target for cancer therapy, Cancer Lett. 266 (2008) 37–52, https://doi.org/10.1016/j.canlet.2008.02.044.

[27] F. Lopes-Coelho, F. Martins, A. Hipólito, et al., The activation of endothelial cells relies on a Ferroptosis-Like mechanism: novel perspectives in management of angiogenesis and cancer therapy, Front Oncol. 11 (2021) 1666, https://doi.org/10.3389/fonc.2021.656229.

[28] U.E. Martinez-Outschoorn, Z. Lin, C. Trimmer, et al., Cancer cells metabolically "fertilize" the tumor microenvironment with hydrogen peroxide, driving the warburg effect: implications for PET imaging of human tumors, Cell Cycle 10 (2011) 2504–2520, https://doi.org/10.4161/cc.10.15.16585.

[29] Y.W. Kim, T.V. Byzova, Oxidative stress in angiogenesis and vascular disease, Blood 123 (2014) 625–631, https://doi.org/10.1182/blood-2013-09-512749.

[30] R. Prieto-Bermejo, A. Hernández-Hernández, The importance of NADPH oxidases and redox signaling in angiogenesis, Antioxidants 6 (2017) 32, https://doi.org/10.3390/antiox6020032.

[31] J. Li, F. Cao, H. liang Yin, et al., Ferroptosis: past, present and future, 11:1–13, Cell Death Dis. 2020 11 (2) (2020), https://doi.org/10.1038/s41419-020-2298-2.

[32] W.S. Yang, R. Sriramaratnam, M.E. Welsch, et al., Regulation of ferroptotic cancer cell death by GPX4, Cell 156 (2014) 317–331, https://doi.org/10.1016/j.cell.2013.12.010.

[33] L.J. Su, J.H. Zhang, H. Gomez, et al., Reactive oxygen Species-Induced lipid peroxidation in apoptosis, autophagy, and ferroptosis, Oxid. Med Cell Longev. 2019 (2019) 1–13, https://doi.org/10.1155/2019/5080843.

[34] P. Lei, T. Bai, Y. Sun, Mechanisms of ferroptosis and relations with regulated cell death: a review, Front Physiol. 10 (2019) 1–13, https://doi.org/10.3389/fphys.2019.00139.

[35] C. Mendes, I. Lemos, A. Hipólito, et al., Metabolic profiling and combined therapeutic strategies unveil the cytotoxic potential of selenium-chrysin (SeChry) in NSCLC cells, Biosci. Rep. 44 (2024) BSR20240752, https://doi.org/10.1042/BSR20240752.

[36] V.M.L. De Sousa, L. Carvalho, Heterogeneity in lung cancer, Pathobiology 85 (2018) 96–107, https://doi.org/10.1159/000487440.

[37] C. Mendes, I. Lemos, I. Francisco, et al., NSCLC presents metabolic heterogeneity, and there is still some leeway for EGF stimuli in EGFR-mutated NSCLC, Lung Cancer 182 (2023) 1–21, https://doi.org/10.1016/j.lungcan.2023.107283.

[38] A.P. Halestrap, The SLC16 gene family - structure, role and regulation in health and disease, Mol. Asp. Med 34 (2013) 337–349, https://doi.org/10.1016/j.mam.2012.05.003.

[39] C. Mendes, J. Serpa, Revisiting lactate dynamics in cancer—a metabolic expertise or an alternative attempt to survive? J. Mol. Med 98 (2020) 1397–1414, https://doi.org/10.1007/s00109-020-01965-0.

[40] K. Elumalai, S. Srinivasan, A. Shanmugam, Review of the efficacy of nanoparticle-based drug delivery systems for cancer treatment, Biomed. Technol. 5 (2024) 109–122, https://doi.org/10.1016/J.BMT.2023.09.001.

[41] C. Pi, W. Zhao, M. Zeng, et al., Anti-lung cancer effect of paclitaxel solid lipid nanoparticles delivery system with curcumin as co-loading partner in vitro and in vivo, Drug Deliv. 29 (2022) 1878–1891, https://doi.org/10.1080/10717544.2022.2086938.

[42] R. Itani, A. Faraj, Al, siRNA conjugated Nanoparticles—A next generation strategy to treat lung cancer, Int J. Mol. Sci. 20 (2019) 6088, https://doi.org/10.3390/ijms20236088.

[43] H. Tang, Z. Zhang, M. Zhu, et al., Efficient delivery of gemcitabine by estrogen Receptor-Targeted PEGylated liposome and its Anti-Lung cancer activity in vivo and in vitro, Pharmaceutics 15 (2023) 988, https://doi.org/10.3390/pharmaceutics15030988.

[44] S. Rawal, S. Khot, V. Bora, et al., Surface-modified nanoparticles of docetaxel for chemotherapy of lung cancer: an intravenous to oral switch, Int J. Pharm. 636 (2023) 122846, https://doi.org/10.1016/j.ijpharm.2023.122846.

[45] J.D. Vanza, R.B. Patel, M.R. Patel, Nanocarrier centered therapeutic approaches: recent developments with insight towards the future in the management of lung cancer, J. Drug Deliv. Sci. Technol. 60 (2020) 102070, https://doi.org/10.1016/j.jddst.2020.102070.

[46] K. Kumar, R. Chawla, Nanocarriers-mediated therapeutics as a promising approach for treatment and diagnosis of lung cancer, J. Drug Deliv. Sci. Technol. 65 (2021) 102677, https://doi.org/10.1016/j.jddst.2021.102677.

[47] M. Habeeb, T.A. Kareem, K.L. Deepthi, et al., Nanomedicine for targeting the lung cancer cells by interpreting the signaling pathways, J. Drug Deliv. Sci. Technol. 77 (2022) 103865, https://doi.org/10.1016/j.jddst.2022.103865.

[48] A.O. Al Khatib, M. El-Tanani, H. Al-Obaidi, Inhaled medicines for targeting Non-Small cell lung cancer, Pharmaceutics 15 (2023) 2777, https://doi.org/10.3390/pharmaceutics15122777.

[49] S. Azarmi, W.H. Roa, R. Löbenberg, Targeted delivery of nanoparticles for the treatment of lung diseases, Adv. Drug Deliv. Rev. 60 (2008) 863–875, https://doi.org/10.1016/j.addr.2007.11.006.

[50] A. Hipólito, C. Mendes, F. Martins, et al., H2S-Synthesizing enzymes are putative determinants in lung cancer management toward personalized Medicine, Antioxidants 13 (2023) 1–29, https://doi.org/10.3390/antiox13010051.

[51] I. Santos, C. Ramos, C. Mendes, et al., Targeting glutathione and cystathionine β-Synthase in ovarian cancer treatment by Selenium-Chrysin polyurea dendrimer nanoformulation, Nutrients 11 (2019) 2523, https://doi.org/10.3390/nu11102523.

[52] R.B. Restani, P.I. Morgado, M.P. Ribeiro, et al., Biocompatible polyurea dendrimers with pH-dependent fluorescence, Angew. Chem. Int. Ed. 51 (2012) 5162–5165, https://doi.org/10.1002/anie.201200362.

[53] K. Yoon, J.M. Harris, M.D. Bentley, Z. Fang, T. Viegas, Multifunctional forms of polyoxazoline copolymers and drug compositions comprising the same, U. S. Pat. 8 (501) (2012) 899.

[54] T.J. Barnes, I. Ametov, C.A. Prestidge, Dendrimer assembly in solution and at interfaces, Int. Conf. Nanosci. Nanotechnol. 278281 2006 (2006), https://doi.org/10.1109/ICONN.2006.340606.

[55] R.B. Restani, J. Conde, R.F. Pires, et al., POxylated polyurea dendrimers: smart Core-Shell vectors with IC50 lowering capacity, Macromol. Biosci. 15 (2015) 1045–1051, https://doi.org/10.1002/mabi.201500131.

[56] R.B. Restani, A.S. Silva, R.F. Pires, et al., Nano-in-Micro POxylated polyurea dendrimers and chitosan dry powder formulations for pulmonary delivery, Part. Part. Syst. Charact. 33 (2016) 851–858, https://doi.org/10.1002/ppsc.201600123.

[57] I.M. El-Sherbiny, H.D.C. Smyth, Controlled release pulmonary administration of curcumin using swellable biocompatible microparticles, Mol. Pharm. 9 (2012) 269–280, https://doi.org/10.1021/MP200351Y/ASSET/IMAGES/MEDIUM/MP-2011-00351Y_0016.GIF.

[58] D.P. Gaspar, M.M. Gaspar, C.V. Eleutério, et al., Microencapsulated solid lipid nanoparticles as a hybrid platform for pulmonary antibiotic delivery, Mol. Pharm. 14 (2017) 2977–2990, https://doi.org/10.1021/acs.molpharmaceut.7b00169.

[59] X. Yao, Y. Zeng, Tumour associated endothelial cells: origin, characteristics and role in metastasis and anti-angiogenic resistance, Front Physiol. 14 (2023) 1199225, https://doi.org/10.3389/fphys.2023.1199225.

[60] F. Houle, J. Huot, Dysregulation of the endothelial cellular response to oxidative stress in cancer, Mol. Carcinog. 45 (2006) 362–367, https://doi.org/10.1002/MC.20218.

[61] I. San-Millán, G.A. Brooks, Reexamining cancer metabolism: lactate production for carcinogenesis could be the purpose and explanation of the warburg effect, Carcinog. 38119133 (2017), https://doi.org/10.1093/carcin/bgw127.

[62] F. Végran, R. Boidot, C. Michiels, et al., Lactate influx through the endothelial cell monocarboxylate transporter MCT1 supports an NF-kB/IL-8 pathway that drives tumor angiogenesis, Cancer Res 71 (2011) 2550–2560, https://doi.org/10.1158/0008-5472.CAN-10-2828.

[63] K. Mitrevska, M.A. Merlos Rodrigo, N. Cernei, et al., Chick chorioallantoic membrane (CAM) assay for the evaluation of the antitumor and antimetastatic activity of platinum-based drugs in association with the impact on the amino acid metabolism, Mater. Today Bio 19 (2023) 100570, https://doi.org/10.1016/j.mtbio.2023.100570.

[64] R.S. Herbst, D. Morgensztern, C. Boshoff, The biology and management of non-small cell lung cancer, Nature 553 (2018) 446–454, https://doi.org/10.1038/nature25183.

[65] J. Tian, X. Wei, W. Zhang, A. Xu, Effects of selenium nanoparticles combined with radiotherapy on lung cancer cells, Front Bioeng. Biotechnol. 8 (2020) 598997, https://doi.org/10.3389/fbioe.2020.598997.

[66] P. Waring, Redox active calcium ion channels and cell death, Arch. Biochem Biophys. 434 (2005) 33–42, https://doi.org/10.1016/j.abb.2004.08.001.

[67] M.S. Ricci, W.-X. Zong, Chemotherapeutic approaches for targeting cell death pathways, Oncologist 11 (2006) 342–357, https://doi.org/10.1634/theoncologist.11-4-342.

[68] X. Xu, Y. Lai, Z.C. Hua, Apoptosis and apoptotic body: disease message and therapeutic target potentials, Biosci. Rep. 39 (2019) 20180992, https://doi.org/10.1042/BSR20180992.

[69] S. Ghosh, R. Yang, D. Duraki, et al., Plasma membrane channel TRPM4 mediates immunogenic Therapy–Induced necrosis, Cancer Res 83 (2023) 3115–3130, https://doi.org/10.1158/0008-5472.CAN-23-0157.
[70] I.L. Martins, C. Charneira, V. Gandin, et al., Selenium-containing chrysin and quercetin derivatives: attractive scaffolds for cancer therapy, J. Med Chem. 58 (2015) 4250–4265, https://doi.org/10.1021/acs.jmedchem.5b00230.
[71] H.T. Endale, W. Tesfaye, T.A. Mengstie, ROS induced lipid peroxidation and their role in ferroptosis, Front Cell Dev. Biol. 11 (2023) 1226044, https://doi.org/10.3389/FCELL.2023.1226044.
[72] W.S. Yang, K.J. Kim, M.M. Gaschler, et al., Peroxidation of polyunsaturated fatty acids by lipoxygenases drives ferroptosis, Proc. Natl. Acad. Sci. USA 113 (2016) E4966–E4975, https://doi.org/10.1073/PNAS.1603244113.
[73] Y. Yu, Y. Yan, F. Niu, et al., Ferroptosis: a cell death connecting oxidative stress, inflammation and cardiovascular diseases, 7, Cell Death Discov. 2021 7 (1) (2021) 193, https://doi.org/10.1038/s41420-021-00579-w.
[74] T. Hirschhorn, B.R. Stockwell, The development of the concept of ferroptosis, Free Radic. Biol. Med 133 (2019) 130–143, https://doi.org/10.1016/j.freeradbiomed.2018.09.043.
[75] J.W. Kim, D.W. Min, D. Kim, et al., GPX4 overexpressed non-small cell lung cancer cells are sensitive to RSL3-induced ferroptosis, 13, Sci. Rep. 2023 13 (1) (2023) 8872, https://doi.org/10.1038/s41598-023-35978-9.
[76] N. Jyotsana, K.T. Ta, K.E. DelGiorno, The role of Cystine/Glutamate antiporter SLC7A11/xCT in the pathophysiology of cancer, Front Oncol. 12 (2022) 858462, https://doi.org/10.3389/fonc.2022.858462.
[77] J. Pei, X. Pan, G. Wei, Y. Hua, Research progress of glutathione peroxidase family (GPX) in redoxidation, Front Pharm. 14 (2023) 1147414, https://doi.org/10.3389/fphar.2023.1147414.
[78] L.P. Zhou, R.J. Zhang, C.Y. Jia, et al., Ferroptosis: a potential target for the intervention of intervertebral disc degeneration, Front Endocrinol. (Lausanne) 13 (2022) 1042060, https://doi.org/10.3389/fendo.2022.1042060.
[79] X. Chen, J. Li, R. Kang, et al., Ferroptosis: machinery and regulation, Autophagy 17 (2021) 2054–2081, https://doi.org/10.1080/15548627.2020.1810918.
[80] X. Chen, P.B. Comish, D. Tang, R. Kang, Characteristics and biomarkers of ferroptosis, Front Cell Dev. Biol. 9 (2021) 637162, https://doi.org/10.3389/FCELL.2021.637162.
[81] S.J. Desai, B. Prickril, A. Rasooly, Mechanisms of phytonutrient modulation of Cyclooxygenase-2 (COX-2) and inflammation related to cancer, Nutr. Cancer 70 (2018) 350–375, https://doi.org/10.1080/01635581.2018.1446091.
[82] H.Y. Tian, B.Y. Huang, H.F. Nie, et al., The interplay between mitochondrial dysfunction and ferroptosis during Ischemia-Associated central nervous system diseases, Brain Sci. 13 (2023), https://doi.org/10.3390/BRAINSCI13101367.
[83] S. Kumfu, S. Chattipakorn, S. Fucharoen, N. Chattipakorn, Mitochondrial calcium uniporter blocker prevents cardiac mitochondrial dysfunction induced by iron overload in thalassemic mice, BioMetals 25 (2012) 1167–1175, https://doi.org/10.1007/S10534-012-9579-X.
[84] J. Khamseekaew, S. Kumfu, S. Wongjaikam, et al., Effects of iron overload, an iron chelator and a T-Type calcium channel blocker on cardiac mitochondrial biogenesis and mitochondrial dynamics in thalassemic mice, Eur. J. Pharm. 799 (2017) 118–127, https://doi.org/10.1016/J.EJPHAR.2017.02.015.
[85] A. Hipólito, C. Mendes, J. Serpa, The metabolic remodelling in lung cancer and its putative consequence in therapy response, Adv. Exp. Med Biol. 1219 (2020) 311–333, https://doi.org/10.1007/978-3-030-34025-4_16.
[86] F. Lopes-Coelho, S. Gouveia-Fernandes, J. Serpa, Metabolic cooperation between cancer and non-cancerous stromal cells is pivotal in cancer progression, Tumor Biol. 40 (2018) 1–15, https://doi.org/10.1177/1010428318756203.
[87] B. Mdkhana, S. Goel, M.A. Saleh, et al., Role of oxidative stress in angiogenesis and the therapeutic potential of antioxidants in breast cancer, Eur. Rev. Med Pharm. Sci. 26 (2022) 4677–4692, https://doi.org/10.26355/eurrev_202207_29192.
[88] E.M. Ragab, D.M. El Gamal, T.M. Mohamed, A.A. Khamis, Therapeutic potential of chrysin nanoparticle-mediation inhibition of succinate dehydrogenase and ubiquinone oxidoreductase in pancreatic and lung adenocarcinoma, Eur. J. Med Res 27 (2022) 172, https://doi.org/10.1186/s40001-022-00803-y.
[89] B. Feng, Y. Zhang, T. Liu, et al., Selenium speciation determines the angiogenesis effect through regulating selenoproteins to trigger ROS-mediated cell apoptosis and cell cycle arrest, Chin. Chem. Lett. 34 (2023) 108264, https://doi.org/10.1016/j.cclet.2023.108264.
[90] S.V. Novoselov, D.F. Calvisi, V.M. Labunskyy, et al., Selenoprotein deficiency and high levels of selenium compounds can effectively inhibit hepatocarcinogenesis in transgenic mice, 24, Oncogene 2005 24 (54) (2005) 8003–8011, https://doi.org/10.1038/sj.onc.1208940.
[91] S.O. Lee, J.Y. Chun, N. Nadiminty, et al., Monomethylated selenium inhibits growth of LNCaP human prostate cancer xenograft accompanied by a decrease in the expression of androgen receptor and prostate-specific antigen (PSA), Prostate 66 (2006) 1070–1075, https://doi.org/10.1002/pros.20329.
[92] M.A. Kato, D.J. Finley, C.C. Lubitz, et al., Selenium decreases thyroid cancer cell growth by increasing expression of GADD153 and GADD34, Nutr. Cancer 62 (2010) 66–73, https://doi.org/10.1080/01635580903191569.
[93] C. Gupta, A. Jaipuria, N. Gupta, Inhalable formulations to treat Non-Small cell lung cancer (NSCLC): recent therapies and developments, Pharmaceutics 15 (2023) 139, https://doi.org/10.3390/pharmaceutics15010139.
[94] K. Knap, K. Kwiecien, K. Reczynska-Kolman, E. Pamula, Inhalable microparticles as drug delivery systems to the lungs in a dry powder formulations, Regen. Biomater. 10 (2023) rbac099, https://doi.org/10.1093/RB/RBAC099.
[95] C. Loira-Pastoriza, J. Todoroff, R. Vanbever, Delivery strategies for sustained drug release in the lungs, Adv. Drug Deliv. Rev. 75 (2014) 81–91, https://doi.org/10.1016/j.addr.2014.05.017.
[96] L.M. Kaminskas, V.M. McLeod, G.M. Ryan, et al., Pulmonary administration of a doxorubicin-conjugated dendrimer enhances drug exposure to lung metastases and improves cancer therapy, J. Control. Release 183 (2014) 18–26, https://doi.org/10.1016/j.jconrel.2014.03.012.
[97] D.S. Conti, D. Brewer, J. Grashik, et al., Poly(amidoamine) dendrimer nanocarriers and their aerosol formulations for siRNA delivery to the lung epithelium, Mol. Pharm. 11 (2014) 1808–1822, https://doi.org/10.1021/MP4006358.
[98] L.N.M. Nguyen, W. Ngo, Z.P. Lin, et al., The mechanisms of nanoparticle delivery to solid tumours, Nat. Rev. Bioeng. 2 (2024) 201–213, https://doi.org/10.1038/s44222-024-00154-9.
[99] Y. Yao, Y. Zhou, L. Liu, et al., Nanoparticle-Based drug delivery in cancer therapy and its role in overcoming drug resistance, Front Mol. Biosci. 7 (2020), https://doi.org/10.3389/FMOLB.2020.00193/PDF.
[100] S. Mazumdar, D. Chitkara, A. Mittal, Exploration and insights into the cellular internalization and intracellular fate of amphiphilic polymeric nanocarriers, Acta Pharm. Sin. B 11 (2021) 903–924, https://doi.org/10.1016/j.apsb.2021.02.019.
[101] M. Murakami, H. Cabral, Y. Matsumoto, et al., Improving drug potency and efficacy by nanocarrier-mediated subcellular targeting, Sci. Transl. Med 3 (2011), https://doi.org/10.1126/SCITRANSLMED.3001385.
[102] O.C. Farokhzad, R. Langer, Impact of nanotechnology on drug delivery, ACS Nano 3 (2009) 16–20, https://doi.org/10.1021/NN900002M.
[103] A. Chakraborty, N.R. Jana, Clathrin to lipid Raft-Endocytosis via controlled surface chemistry and efficient perinuclear targeting of nanoparticle, J. Phys. Chem. Lett. 6 (2015) 3688–3697, https://doi.org/10.1021/ACS.JPCLETT.5B01739.
[104] N.D. Donahue, H. Acar, S. Wilhelm, Concepts of nanoparticle cellular uptake, intracellular trafficking, and kinetics in nanomedicine, Adv. Drug Deliv. Rev. 143 (2019) 68–96, https://doi.org/10.1016/j.addr.2019.04.008.
[105] J.P. Smith, A.L. Uhernik, L. Li, et al., Regulation of Mct1 by cAMP-dependent internalization in rat brain endothelial cells, Brain Res 1480 (2012) 1–11, https://doi.org/10.1016/J.BRAINRES.2012.08.026.
[106] J. Peper, D. Kownatzki-Danger, G. Weninger, et al., Caveolin3 stabilizes McT1-Mediated Lactate/Proton transport in cardiomyocytes, Circ. Res 128 (2021) E102–E120, https://doi.org/10.1161/CIRCRESAHA.119.316547.
[107] L. Wu, M. Liu, W. Shan, et al., Bioinspired butyrate-functionalized nanovehicles for targeted oral delivery of biomacromolecular drugs, J. Control. Release 262 (2017) 273–283, https://doi.org/10.1016/J.JCONREL.2017.07.045.
[108] A. Cruz, P. Mota, C. Ramos, et al., Polyurea dendrimer Folate-Targeted nanodelivery of l-Buthionine sulfoximine as a tool to tackle ovarian cancer chemoresistance, Antioxid. (Basel) 9 (2020), https://doi.org/10.3390/antiox9020133.
[109] I. Martínez-Reyes, N.S. Chandel, Mitochondrial TCA cycle metabolites control physiology and disease, 11, Nat. Commun. 2020 11 (1) (2020) 102, https://doi.org/10.1038/s41467-019-13668-3.
[110] J. Zhang, Y. Zheng, L. Martens, A.F.H. Pfeiffer, The regulation and secretion of glucagon in response to nutrient composition: unraveling their intricate mechanisms, Nutrients 15 (2023) 3913, https://doi.org/10.3390/nu15183913.
[111] M.C. Egbujor, O.T. Olaniyan, C.N. Emeruwa, et al., An insight into role of amino acids as antioxidants via NRF2 activation, 56, Amino Acids 2024 56 (1) (2024) 23, https://doi.org/10.1007/S00726-024-03384-8.
[112] S. Facchin, L. Bertin, E. Bonazzi, et al., Short-Chain fatty acids and human health: from metabolic pathways to current therapeutic implications, Life 14 (2024) 559, https://doi.org/10.3390/life14050559.